arXiv:1302.1594v1 [physics.flu-dyn] 6 Feb 2013

Model-based scaling and prediction of the streamwise energy intensity in high-Reynolds number turbulent channels

By Rashad Moarref[1], Ati S. Sharma[2], Joel A. Tropp[3] AND Beverley J. McKeon[1]

[1]Graduate Aerospace Laboratories, California Institute of Technology, CA 91125, USA
[2]Automatic Control & Systems Engineering, University of Sheffield, S1 3JD, UK
[3]Computing & Mathematical Sciences, California Institute of Technology, CA 91125, USA

We study the Reynolds number scaling of a gain-based, low-rank approximation to turbulent channel flows, determined by the resolvent formulation of McKeon & Sharma (2010), in order to obtain a description of the streamwise turbulence intensity from direct consideration of the Navier-Stokes equations. Under this formulation, the velocity field is decomposed into propagating waves (with single streamwise and spanwise wavelengths and wave speed) whose wall-normal shapes are determined from the principal singular function of the corresponding resolvent operator. We establish that the resolvent formulation admits three classes of wave parameters that induce universal behavior with Reynolds number on the low-rank model, and which are consistent with scalings proposed throughout the wall turbulence literature. For the rank-1 model subject to broadband forcing, the integrated streamwise energy density takes a universal form which is consistent with the dominant near-wall turbulent motions. When the shape of the forcing is optimized to enforce matching with results from direct numerical simulations at low turbulent Reynolds numbers, further similarity appears. Representation of these weight functions using similarity laws enables prediction of the Reynolds number and wall-normal variations of the streamwise energy intensity at high Reynolds numbers ($Re_\tau \approx 10^3 - 10^{10}$). Results from this low rank model of the Navier-Stokes equations compare favorably with experimental results in the literature.

1. Introduction

Understanding the behavior of wall-bounded turbulent flows at high Reynolds numbers has tremendous technological implications, for example, in air and water transportation. This problem has received significant attention over the last two decades especially in the light of full-field flow information revealed by direct numerical simulations (DNS) at relatively small Reynolds numbers and high-Reynolds number experiments. Notwithstanding the recent developments, the highest Reynolds numbers that are considered in DNS are an order of magnitude smaller than experiments, which are in turn conducted at Reynolds numbers that are typically two orders of magnitude smaller than most applications. This creates a critical demand for model-based approaches that describe and predict the behavior of turbulent flows at technologically relevant Reynolds numbers.

Wall turbulence has been the topic of several reviews; see, for example, Robinson (1991); Adrian (2007) for structure of coherent motions, Gad-El-Hak & Bandyopadhyay

(1994) for turbulence statistics and scaling issues, Panton (2001) for self-sustaining turbulence mechanisms, and Klewicki (2010); Marusic *et al.* (2010*c*); Smits *et al.* (2011) for the latest findings and main challenges in examining high-Reynolds number wall turbulence. In the present study, special attention is paid to scaling and universality of the turbulent energy spectra at high Reynolds numbers. We also note that the energy spectra exhibit clear signatures of coherent turbulent motions such as the near-wall streaks, the large-scale motions (LSMs), and the very large-scale motions (VLSMs).

1.1. *Overview of dominant coherent motions*

In the interests of giving a brief overview of the energetically dominant coherent motions in wall turbulence, we will review three classes of structure. The near-wall system of quasi-streamwise streaks and counter-rotating vortices with streamwise length and spanwise spacing of approximately 1000 and 100 inner (viscous) units, centered at approximately 15 inner units above the wall, has been well-studied. These ubiquitous features of wall turbulence are responsible for large production of turbulent kinetic energy (Kline *et al.* 1967; Smith & Metzler 1983).

Another commonly-observed feature of turbulent flows is the hairpin vortex. In low Reynolds number flows, at least, packets of hairpin vortices have been observed to extend from the wall to the edge of the boundary layer and constitute LSMs (Head & Bandyopadhyay 1981; Adrian *et al.* 2000; Adrian 2007), with streamwise extent approximately 2-3 outer units (channel half-height, pipe radius, or the boundary layer thickness).

VLSMs have been observed to reside in the logarithmic region of the turbulent mean velocity, with lengths of approximately 10-15 outer units in boundary layers and up to 30 outer units in channels and pipes (see, for example, Kim & Adrian 1999; Balakumar & Adrian 2007; Monty *et al.* 2007). The emergence of VLSMs was originally attributed to alignment of LSMs (Kim & Adrian 1999). However, Smits *et al.* (2011) concluded that this is unlikely since the detached LSMs are located at a farther distance from the wall than the VLSMs and the attached LSMs have much smaller width than VLSMs and are convected at different speeds. Recently, the correlation between the envelope of small scale activity and the large scale velocity signal (identified via filtering in spectral space), which has been interpreted as an amplitude modulation of the small scales, has been investigated in detail, e.g. Hutchins & Marusic (2007*b*); Mathis *et al.* (2009*a*,*b*); Chung & McKeon (2010); Hutchins *et al.* (2011).

1.2. *Overview of scaling issues*

In spite of recent advances in understanding the structure of wall turbulence, the Reynolds number scaling of the turbulent energy spectra and the energy intensities remains an open area of research. The main experimental obstacle is maintaining the necessary spatial resolution for measurement accuracy while achieving the high Reynolds numbers required for large separation between the small and large turbulent scales. For example, the available experiments are performed at relatively small friction Reynolds numbers, $Re_\tau \approx \mathcal{O}(10^4)$, with a notable exception of the atmospheric surface layer measurements of, e.g., Metzger & Klewicki (2001) ($Re_\tau \approx \mathcal{O}(10^6)$) that are in turn generally contaminated by surface roughness effects. Most high-Reynolds number experiments suffer from spatial resolution issues in the inner region (see, for example, Hutchins *et al.* 2009).

Significant experimental effort has been devoted to determining the behavior of the streamwise energy intensity at high Reynolds numbers since it dominates the turbulent kinetic energy and is easier to measure relative to the wall-normal and spanwise velocities. It is understood that both small and large scales contribute to the streamwise energy intensity (Metzger & Klewicki 2001; Marusic & Kunkel 2003; Hutchins & Marusic 2007*a*;

Marusic *et al.* 2010*a*). It is well-known that a region of the streamwise wavenumber spectrum scales with inner units; Marusic *et al.* (2010*a*) showed by filtering that the contribution of such scales to the streamwise energy intensity, and therefore by extension also the streamwise spectrum, is universal, i.e. independent of Reynolds number. On the other hand, the large motions have been shown to scale in outer units (Kim & Adrian 1999); Mathis *et al.* (2009*a*) proposed that the corresponding peak in streamwise intensity occurs close to the geometric mean of the limits of the logarithmic region in the turbulent mean velocity. The amplitude of this energetic peak increases with Reynolds number and has a footprint down to the wall (Hutchins & Marusic 2007*b*). Note however, that available data are not sufficiently well-resolved to determine unequivocally the Reynolds number scaling of either the inner or outer peaks of the streamwise energy intensity (see, for example, Marusic *et al.* 2010*a*).

Theoretical approaches also offer insight into the scaling of the spectrum with increasing Reynolds numbers, originating with the attached eddy concepts described by Townsend (1976). Perry & Chong (1982) developed these ideas to include hierarchies of geometrically similar, attached eddies in the logarithmic region, and formulated a model for the distribution of eddies that was required to capture characteristics including the mean velocity and streamwise turbulence intensity profiles. Subsequent works by Perry and co-authors extended this formulation beyond the wall region; most recently Marusic & Kunkel (2003) used empirical scaling arguments concerning the effective forcing of the outer turbulence on the viscous region to propose a similarity expression for the streamwise energy intensity that is valid throughout the zero pressure boundary layer. More recently, Marusic *et al.* (2010*b*) outlined an observationally-based, predictive formulation for the variation of the streamwise turbulent intensity up to the geometric mean of the logarithmic region based on consideration of the correlation between large and small scales.

1.3. *Review of previous model-based approaches*

We seek in this work a description of the streamwise turbulence intensity for all wall-normal locations arising from direct consideration, and modeling, of the Navier-Stokes equations. There has been much work in this vein, highlighting several important features of the Navier-Stokes equations. We provide a brief review of the most relevant literature here.

It is understood that high sensitivity of the Navier-Stokes equations (NSE) linearized around the laminar velocity provides alternative paths to transition that bypass linear instability; see, for example, Schmid & Henningson (2001). Trefethen *et al.* (1993) showed that the high flow sensitivity is related to non-normality of the coupled Orr-Sommerfeld and Squire operators; see also Schmid (2007). These operators are coupled in the presence of mean shear and spanwise-varying fluctuations. Physically, as originally explained by Landahl (1975), a large streamwise disturbance is induced on the flow in response to lift-up of a fluid particle by the wall-normal velocity such that its wall-parallel momentum is conserved.

Even in linearly stable flows, the high sensitivity can result in large transient responses, meaning that the energy of certain initial perturbations significantly grows before eventual decay to zero (Gustavsson 1991; Klingmann 1992; Butler & Farrell 1992; Schmid & Henningson 1992; Reddy & Henningson 1993). In addition, the high sensitivity is responsible for high energy amplification, meaning that the velocity fluctuations achieve a large variance at the steady state for the flow subject to zero-mean stochastic disturbances (Farrell & Ioannou 1993*b*; Bamieh & Dahleh 2001; Jovanović & Bamieh 2005). The dominant structures that emerge from the above transient growth and energy am-

plification analyses are reminiscent of the streamwise streaks observed at the early stages of transition to turbulence (Matsubara & Alfredsson 2001). They are characterized by infinitely long spanwise-periodic regions of high and low streamwise velocity surrounded by pairs of counter-rotating streamwise vortices that are separated by approximately 3.5 outer units.

The critical role of linear amplification mechanism in promoting and maintaining turbulent flows was highlighted in direct numerical simulations of Kim & Lim (2000). It is known that the NSE linearized around the turbulent mean velocity are stable for all Reynolds numbers (Malkus 1956). Early model-based approaches extended the aforementioned sensitivity analyses of the laminar flow to the turbulent channel flow and found dominance of streamwise streaks that are spaced by 3 outer units, which is approximately the same as in the laminar flow. In addition to the outer-scaled dominant structures, Butler & Farrell (1993); Farrell & Ioannou (1993*a*) showed that the largest transient response over an eddy turnover time of 80 inner units, associated with the near-wall cycle, is obtained for initial perturbations that are infinitely long and have the same spanwise spacing as the near-wall streaks, i.e. 100 inner units. The same streamwise and spanwise lengths were obtained in flows subject to stochastic disturbances over a coherence time of 90 inner units (Farrell & Ioannou 1998).

Reynolds & Hussain (1972) put forward a modified linear model to account for the effect of background Reynolds stresses on the velocity fluctuations. They proposed to augment the molecular viscosity by the turbulent eddy viscosity that is required to maintain the mean velocity. This model yields two local optima for the structures with largest transient growth (del Álamo & Jiménez 2006; Pujals *et al.* 2009) and energy amplification (Hwang & Cossu 2010) without the need for confining the optimization time. These peaks correspond to streamwise-elongated structures with a spacing of 80 inner units and 3-4 outer units and are in fair agreement with the spacing of near-wall streaks and the very large-scale motions in real turbulent flows.

An exact representation of the NSE was introduced by McKeon & Sharma (2010) in which (i) a set of linear sub-systems describe extraction of energy from the mean velocity at individual wavenumbers/frequencies; and (ii) the only source of coupling between these sub-systems is the conservative nonlinear interaction of their outputs, that determines both the input to the sub-systems and the turbulent mean velocity. At its heart is the ability to analyze the flow of energy from the mean velocity to all the velocity scales and identify the essential linear amplification and nonlinear redistribution mechanisms that drive the turbulent flow. The input-output relationship of the linear sub-systems can be described by transfer functions whose low-rank nature in the wall-normal direction enables significant simplification of their analysis.

One of the main differences between the formulation of McKeon & Sharma (2010) and other input-output analyses of laminar and turbulent flows (see, for example, Jovanović & Bamieh 2005; Hwang & Cossu 2010) is parameterization of the waves with wave speed rather than temporal frequency. While the latter approaches conclude that the globally optimal transient growth and energy amplification takes place for zero streamwise wavenumber and temporal frequency, they do not provide guidelines for finding locally (in wall-normal direction) optimal wave parameters. On the other hand, selecting the wave speed (i) enables systematical search for both locally and globally optimal wave shapes and parameters; (ii) removes the ambiguity about the wave speed corresponding to the globally optimal waves by determining the limit of the ratio between zero streamwise wavenumber and temporal frequency; and (iii) distinguishes between non-normality and criticality as the main linear amplification mechanisms.

McKeon & Sharma (2010) showed that the principal forcing and response directions

associated with the linear sub-systems are consistent with the dominant response shapes in real turbulent pipe flows. In addition, the low-dimensional and sparse feature of the resulting model enables development and utilization of compressive sampling techniques for analyzing the turbulent flow dynamics (Bourguignon *et al.* 2013). This formulation has also proven useful for pre- and post-diction of experimental observations in turbulent pipe flow (Sharma & McKeon 2012; McKeon *et al.* 2013).

1.4. *Paper outline*

In this paper, we identify the Reynolds number scaling of a low-rank approximation to turbulent channel flow and utilize it for predicting the streamwise energy intensity at high Reynolds numbers. Our development is outlined as follows: In § 2, we briefly review the resolvent formulation, highlight its low-rank nature, and show that a rank-1 approximation captures the most energetic modes of real turbulent channels. The stage is set for studying the energy density of fluctuations using a minimum number of assumptions by considering a rank-1 model in the wall-normal direction subject to broadband forcing in the wall-parallel directions and time. Furthermore, a summary of the computational approach for determining the rank-1 model is provided.

Three classes of wave parameters for which the low-rank approximation of the resolvent exhibits universal behavior (independence) with Reynolds number are identified in § 3. The requirement for universality highlights the role of wave speed in distinguishing these classes. Each class of waves is characterized by a unique range of wave speeds and a unique spatial scaling that emerge from the resolvent. For the rank-1 model subject to broadband forcing, we reveal the universal streamwise energy densities, and show that the peaks of these energy densities roughly agree with the most energetic turbulent motions, i.e. the near-wall streaks, the VLSMs, and the LSMs.

In § 4, we show that the streamwise energy density of the rank-1 model with broadband forcing can be optimally weighted as a function of wave speed to match the intensity of simulations at low turbulent Reynolds numbers. The weight functions are then formulated using similarity laws which, in conjunction with the universal energy densities, enable prediction of the streamwise energy intensity at high Reynolds numbers. The paper is concluded in § 5 and several future directions are discussed.

2. Low-rank approximation to channel flow

An overview of the rationale for considering a low rank approximation to turbulent channel flow is presented in this section. We follow the development of McKeon & Sharma (2010) for turbulent pipe flow, showing that equivalent results are obtained for channels and highlighting the new observations. The pressure-driven flow of an incompressible Newtonian fluid is governed by the nondimensional NSE and the continuity constraint

$$\begin{aligned} \mathbf{u}_t + (\mathbf{u}\cdot\nabla)\mathbf{u} + \nabla P &= (1/Re_\tau)\Delta\mathbf{u}, \\ \nabla\cdot\mathbf{u} &= 0, \end{aligned} \tag{2.1}$$

where $\mathbf{u}(x,y,z,t)$ is the velocity vector, $P(x,y,z,t)$ is the pressure, ∇ is the gradient operator, and $\Delta = \nabla\cdot\nabla$ is the Laplacian. The streamwise and spanwise directions, x and z, are infinitely long, the wall-normal direction is finite, $0 \le y \le 2$, and t denotes time; see figure 1(a) for the geometry. The subscript t represents temporal derivatives, e.g. $\mathbf{u}_t = \partial\mathbf{u}/\partial t$. The Reynolds number $Re_\tau = u_\tau h/\nu$ is defined based on the channel half-height h, kinematic viscosity ν, and friction velocity $u_\tau = \sqrt{\tau_w/\rho}$, where τ_w is the shear stress at the wall, and ρ is the density. Velocity is normalized by u_τ, spatial variables

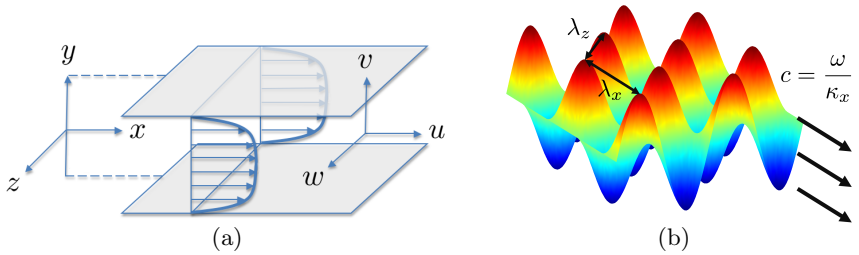

FIGURE 1. (a) Pressure driven channel flow; and (b) Schematic of a two-dimensional propagating wave with streamwise and spanwise wavelengths λ_x and λ_z and streamwise propagating speed c.

by h, time by h/u_τ, and pressure by ρu_τ^2. The spatial variables are denoted by $^+$ when normalized by the viscous length scale ν/u_τ, e.g. $y^+ = Re_\tau y$.

2.1. *Decomposition in homogenous directions*

The velocity is decomposed using the Fourier transform in the homogenous directions and time

$$\mathbf{u}(x,y,z,t) \;=\; \iiint_{-\infty}^{\infty} \hat{\mathbf{u}}(y;\kappa_x,\kappa_z,\omega)\, \mathrm{e}^{\mathrm{i}(\kappa_x x+\kappa_z z-\omega t)} \mathrm{d}\kappa_x\, \mathrm{d}\kappa_z\, \mathrm{d}\omega, \tag{2.2}$$

where $\hat{}$ denotes a variable in the transformed domain, and the triplet $(\kappa_x,\kappa_z,\omega)$ is the streamwise and spanwise wavenumbers and the temporal (angular) frequency. For any $(\kappa_x,\kappa_z,\omega)\neq 0$, $\hat{\mathbf{u}}(y;\kappa_x,\kappa_z,\omega)$ represents a propagating wave with streamwise and spanwise wavelengths $\lambda_x = 2\pi/\kappa_x$ and $\lambda_z = 2\pi/\kappa_z$ and speed $c = \omega/\kappa_x$ in the streamwise direction; see figure 1(b) for an illustration. Some special cases include standing waves ($c = 0$), infinitely long waves ($\kappa_x = 0$), and infinitely wide waves ($\kappa_z = 0$). In this study, we emphasize the eminent role of wave speed, a factor that was highlighted by McKeon & Sharma (2010) while being predominantly neglected in the previous studies, in determining the classes of propagating waves that are universal with Reynolds number.

The turbulent mean velocity $\mathbf{U}(y) = [U(y)\ 0\ 0]^T = \hat{\mathbf{u}}(y;0,0,0)$ corresponds to $(\kappa_x,\kappa_z,\omega) = 0$ and is assumed to be known. McKeon & Sharma (2010) avoided the closure problem for the mean velocity by using $U(y)$ obtained in pipe flow experiments, but note that the resolvent formulation could be used to determine the mean velocity profile, a topic of ongoing work (see McKeon *et al.* 2013). Here, we use a semi-empirical turbulent viscosity model, originally proposed for pipe flow (Malkus 1956; Cess 1958) and extended to channel flow (Reynolds & Tiederman 1967), to determine $U(y)$

$$\begin{aligned} U(y) \;&=\; Re_\tau \int_0^y \frac{1-\xi}{1+\nu_T(\xi)}\,\mathrm{d}\xi, \\ \nu_T(y) \;&=\; \frac{1}{2}\left\{1+\left(\frac{\kappa Re_\tau}{3}\left(2y-y^2\right)\left(3-4y+2y^2\right)\left\{1-\mathrm{e}^{\left(|y-1|-1\right)\frac{Re_\tau}{\alpha}}\right\}\right)^2\right\}^{1/2} - \frac{1}{2}, \end{aligned} \tag{2.3}$$

where ν_T is normalized by ν, and the parameters α and κ appear in the van Driest's wall law and the von Kármán log law. These parameters are obtained by minimizing the deviation between $U(y)$ in (2.3) and the DNS-based turbulent mean velocity profile. The α and κ obtained by Moarref & Jovanović (2012) suggest that both of these values converge for large Re_τ. We take $\alpha = 25.4$ and $\kappa = 0.426$ for all Reynolds numbers and

note that these values are optimized for $Re_\tau = 2003$ (del Álamo & Jiménez 2006; Pujals *et al.* 2009).

Following McKeon & Sharma (2010), the convective nonlinearity in (2.1) is considered as a forcing term $\mathbf{f} = -(\mathbf{u}\cdot\nabla)\mathbf{u}$ that drives the velocity fluctuations. For any $(\kappa_x, \kappa_z, \omega) \neq 0$, an equation for velocity fluctuations $\hat{\mathbf{u}}(y;\kappa_x,\kappa_z,\omega) = [\,\hat{u}\ \hat{v}\ \hat{w}\,]^T$ around the turbulent mean velocity is obtained by substituting (2.2) in (2.1), and using the orthonormality of the complex exponential functions

$$\begin{aligned} -\mathrm{i}\omega\hat{\mathbf{u}} + (\mathbf{U}\cdot\nabla)\hat{\mathbf{u}} + (\hat{\mathbf{u}}\cdot\nabla)\mathbf{U} + \nabla\hat{p} - (1/Re_\tau)\Delta\hat{\mathbf{u}} &= \hat{\mathbf{f}}, \\ \nabla\cdot\hat{\mathbf{u}} &= 0. \end{aligned} \tag{2.4}$$

Here, $\nabla = [\,\mathrm{i}\kappa_x\ \partial_y\ \mathrm{i}\kappa_z\,]^T$, $\Delta = \partial_{yy} - \kappa^2$ with $\kappa^2 = \kappa_x^2 + \kappa_z^2$, and

$$\hat{\mathbf{f}}(y;\kappa_x,\kappa_z,\omega) = [\,\hat{f}_1\ \hat{f}_2\ \hat{f}_3\,]^T = \\ -\iiint_{\substack{(\kappa_x',\kappa_z',\omega')\neq(0,0,0)\\(\kappa_x',\kappa_z',\omega')\neq(\kappa_x,\kappa_z,\omega)}} (\hat{\mathbf{u}}(y;\kappa_x',\kappa_z',\omega')\cdot\nabla)\,\hat{\mathbf{u}}(y;\kappa_x-\kappa_x',\kappa_z-\kappa_z',\omega-\omega')\,\mathrm{d}\kappa_x'\,\mathrm{d}\kappa_z'\,\mathrm{d}\omega'. \tag{2.5}$$

McKeon & Sharma (2010) implicitly accounted for the continuity constraint by projecting the velocity field onto the divergence-free basis of Meseguer & Trefethen (2003). Here, we use a standard choice of wall-normal velocity $\hat{v}$ and wall-normal vorticity $\hat{\eta} = \mathrm{i}\kappa_z\hat{u} - \mathrm{i}\kappa_x\hat{w}$ as the state variables, $\hat{\boldsymbol{\zeta}}(y;\kappa_x,\kappa_z,\omega) = [\,\hat{v}\ \ \hat{\eta}\,]^T$, to eliminate the pressure term and the continuity constraint from (2.4) and obtain

$$\begin{aligned} -(\mathrm{i}\omega I + A(\kappa_x,\kappa_z))\,\hat{\boldsymbol{\zeta}}(y;\kappa_x,\kappa_z,\omega) &= C^\dagger(\kappa_x,\kappa_z)\,\hat{\mathbf{f}}(y;\kappa_x,\kappa_z,\omega), \\ \hat{\mathbf{u}}(y;\kappa_x,\kappa_z,\omega) &= C(\kappa_x,\kappa_z)\,\hat{\boldsymbol{\zeta}}(y;\kappa_x,\kappa_z,\omega). \end{aligned} \tag{2.6}$$

Here, A is the state operator, C maps the state vector to the velocity vector, and the adjoint of C (denoted by $C^\dagger$) maps the forcing vector to the state vector. A, B, and C are operators in y and parameterized by κ_x and κ_z; see (3.1), to be discussed later. The input-output relationship between $\hat{\mathbf{f}}$ and $\hat{\mathbf{u}}$ is obtained upon elimination of $\hat{\boldsymbol{\zeta}}$ from (2.6)

$$\begin{aligned} \hat{\mathbf{u}}(y;\kappa_x,\kappa_z,\omega) &= H(\kappa_x,\kappa_z,\omega)\,\hat{\mathbf{f}}(y;\kappa_x,\kappa_z,\omega), \\ H(\kappa_x,\kappa_z,\omega) &= C(\kappa_x,\kappa_z)R_A(\kappa_x,\kappa_z,\omega)C^\dagger(\kappa_x,\kappa_z), \end{aligned} \tag{2.7}$$

where $R_A(\kappa_x,\kappa_z,\omega) = -(\mathrm{i}\omega I + A(\kappa_x,\kappa_z))^{-1}$ is the resolvent of A. As illustrated in figure 2, the only source of coupling between propagating waves with different wavenumbers is the quadratic dependence of $\mathbf{f}(x,y,z,t)$ on $\mathbf{u}(x,y,z,t)$. For any wavenumber triplet, the input-output map from $\hat{\mathbf{f}}$ to $\hat{\mathbf{u}}$ (shown by the dashed rectangle) represents a sub-unit of the full NSE.

2.2. *Decomposition in the wall-normal direction*

The transfer function $H(\kappa_x,\kappa_z,\omega)$ provides a large amount of information about the input-output relationship between $\hat{\mathbf{f}}$ and $\hat{\mathbf{u}}$. Following the gain analysis of McKeon & Sharma (2010), we use the Schmidt (singular value) decomposition to provide a wall-

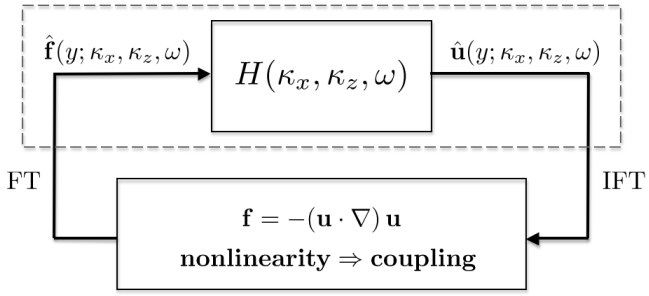

FIGURE 2. For any triplet $(\kappa_x,\kappa_z,\omega)$, the operator $H(\kappa_x,\kappa_z,\omega)$ maps the forcing $\hat{\mathbf{f}}$ to the response $\hat{\mathbf{u}}$. The different wavenumbers are coupled via the quadratic relationship between $\mathbf{f}(x,y,z,t)$ and $\mathbf{u}(x,y,z,t)$. FT and IFT stand for Fourier transform and inverse Fourier transform, respectively. The input-output map (shown with the dashed rectangle) is the main focus of the present study.

normal basis based on the most highly amplified forcing and response directions:

$$\begin{aligned}\hat{\mathbf{u}}(y;\kappa_x,\kappa_z,\omega) &= H(\kappa_x,\kappa_z,\omega)\,\hat{\mathbf{f}}(y;\kappa_x,\kappa_z,\omega)\\ &= \sum_{j=1}^{\infty}\sigma_j(\kappa_x,\kappa_z,\omega)\,a_j(\kappa_x,\kappa_z,\omega)\,\hat{\boldsymbol{\psi}}_j(y;\kappa_x,\kappa_z,\omega),\\ a_j(\kappa_x,\kappa_z,\omega) &= \int_{-1}^{1}\hat{\boldsymbol{\phi}}_j^{*}(y;\kappa_x,\kappa_z,\omega)\,\hat{\mathbf{f}}(y;\kappa_x,\kappa_z,\omega)\,\mathrm{d}y,\end{aligned}\tag{2.8}$$

where $\sigma_1\geq\sigma_2\geq\cdots>0$ denote the singular values of H, and the singular functions $\hat{\boldsymbol{\phi}}_j=[\,\hat{f}_{1j}\;\hat{f}_{2j}\;\hat{f}_{3j}\,]^T$ and $\hat{\boldsymbol{\psi}}_j=[\,\hat{u}_j\;\hat{v}_j\;\hat{w}_j\,]^T$ are respectively the forcing and response directions corresponding to σ_j.

While the singular values of H are unique, additional treatment is necessary to obtain unique singular functions. Unlike in a pipe, the singular values come in pairs due to the wall-normal symmetry in the channel; see, for example, figure 4(a). The paired singular values are equal unless both the streamwise and spanwise wavelengths are large relative to the channel height ($\mathcal{O}(\lambda_x)\gtrsim 1$ and $\mathcal{O}(\lambda_z)\gtrsim 1$). When the paired singular values are different, unique singular functions can be obtained modulo a complex multiplicative constant of unit magnitude if an orthonormality constraint is imposed on them

$$\int_{-1}^{1}\hat{\boldsymbol{\phi}}_j^{*}(y;\kappa_x,\kappa_z,\omega)\,\hat{\boldsymbol{\phi}}_k(y;\kappa_x,\kappa_z,\omega)\,\mathrm{d}y \;=\; \int_{-1}^{1}\hat{\boldsymbol{\psi}}_j^{*}(y;\kappa_x,\kappa_z,\omega)\,\hat{\boldsymbol{\psi}}_k(y;\kappa_x,\kappa_z,\omega)\,\mathrm{d}y \;=\; \delta_{jk},\tag{2.9}$$

where δ denotes the Kronecker delta. In the case where the paired singular values are equal, we impose a symmetry/anti-symmetry constraint on the singular functions in addition to the above orthonormality constraint. In other words, the corresponding singular functions assume the same magnitude throughout the channel while being in phase in one half of the channel and out of phase in the other half.

In this study, we select the unknown multiplicative constant (after orthonormalization) such that $\hat{u}_j(y_{\max};\kappa_x,\kappa_z,\omega)$ is a real number at the wall-normal location $y_{\max}$ where the absolute value of $\hat{u}_j$ is the largest. This choice places the maximum of $u_j(x,y,z,t;\kappa_x,\kappa_z,\omega)$ at the origin $x=z=t=0$. The channel symmetries in the streamwise and spanwise

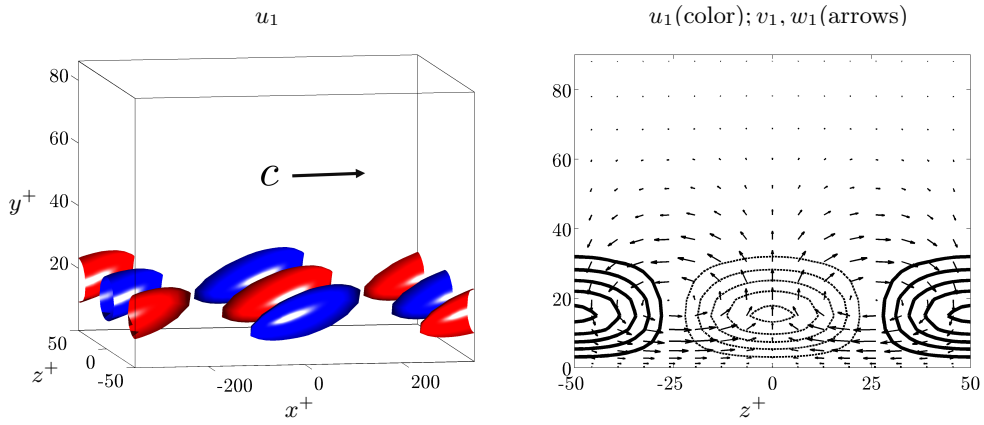

FIGURE 3. The principal velocity response $\boldsymbol{\psi}_1(x, y, z, t; \kappa_x, \kappa_z, \omega) = [\, u_1 \;\; v_1 \;\; w_1 \,]^T$ for $\lambda_x^+ = 700$, $\lambda_z^+ = 100$, $c = 10$, and $Re_\tau = 10000$ at $t = 0$. (Left) The isosurfaces of the streamwise velocity at 60% of its maximum; (Right) The streamwise velocity (contours) and the spanwise and wall-normal velocity (arrows) at $x^+ = \lambda_x^+/2$. The contours in (b) represent positive (thick solid) and negative (thin dashed) values from 3 to 15 with increments of 3.

directions can be used to obtain u_j, v_j, and w_j in the physical domain

$$\begin{aligned} u_j(x, y, z, t; \kappa_x, \kappa_z, \omega) &= 4\cos(\kappa_z z)\,\mathrm{Re}\left(\hat{u}_j(y; \kappa_x, \kappa_z, \omega)\, \mathrm{e}^{\mathrm{i}(\kappa_x x - \omega t)}\right), \\ v_j(x, y, z, t; \kappa_x, \kappa_z, \omega) &= 4\cos(\kappa_z z)\,\mathrm{Re}\left(\hat{v}_j(y; \kappa_x, \kappa_z, \omega)\, \mathrm{e}^{\mathrm{i}(\kappa_x x - \omega t)}\right), \\ w_j(x, y, z, t; \kappa_x, \kappa_z, \omega) &= -4\sin(\kappa_z z)\,\mathrm{Im}\left(\hat{w}_j(y; \kappa_x, \kappa_z, \omega)\, \mathrm{e}^{\mathrm{i}(\kappa_x x - \omega t)}\right), \end{aligned}$$

where Re and Im denote the real and imaginary parts of a complex number. The representation of the forcing directions in the physical domain is obtained using similar expressions.

From the singular value decomposition (2.8) and the orthonormality constraints (2.9) it follows that if the forcing is aligned in the $\hat{\boldsymbol{\phi}}_j$ direction with unit energy, the response is aligned in the $\hat{\boldsymbol{\psi}}_j$ direction with energy σ_j^2. Consequently, the forcing and response directions with the largest gain correspond to the principal singular functions $\hat{\boldsymbol{\phi}}_1$ and $\hat{\boldsymbol{\psi}}_1$. For any $(\kappa_x, \kappa_z, \omega)$, the singular functions of H should be thought of as propagating waves in the physical domain.

Equivalent near-wall structures to those reported for pipe flows by McKeon & Sharma (2010); McKeon *et al.* (2013) are obtained for channel flows. For example, the principal singular function $\boldsymbol{\psi}_1(x, y, z, t; \kappa_x, \kappa_z, \omega) = [\, u_1 \;\; v_1 \;\; w_1 \,]^T$ for the propagating wave corresponding to the energetic near-wall cycle ($\lambda_x^+ = 700$, $\lambda_z^+ = 100$, $c = U(y^+ = 15) = 10$) for $Re_\tau = 10000$ is shown in figure 3. The streamwise component of these structures contains regions of fast- and slow- moving fluids that are aligned in the streamwise direction, slightly inclined to the wall, and are sandwiched between counter-rotating vortical motions in the cross-stream plane.

2.3. *Low-rank nature of H*

The operator H, acting on functions of y, can be described as low-rank if a significant portion of its response to a broadband forcing in y is captured by projection on the first few response directions. McKeon & Sharma (2010) highlighted the low-rank nature of H for turbulent pipe flow. Figure 4(a) shows the first twenty singular values of H for $\lambda_x^+ = 700$, $\lambda_z^+ = 100$, and $c = 10$ in turbulent channel flow with $Re_\tau = 2003$. We see that

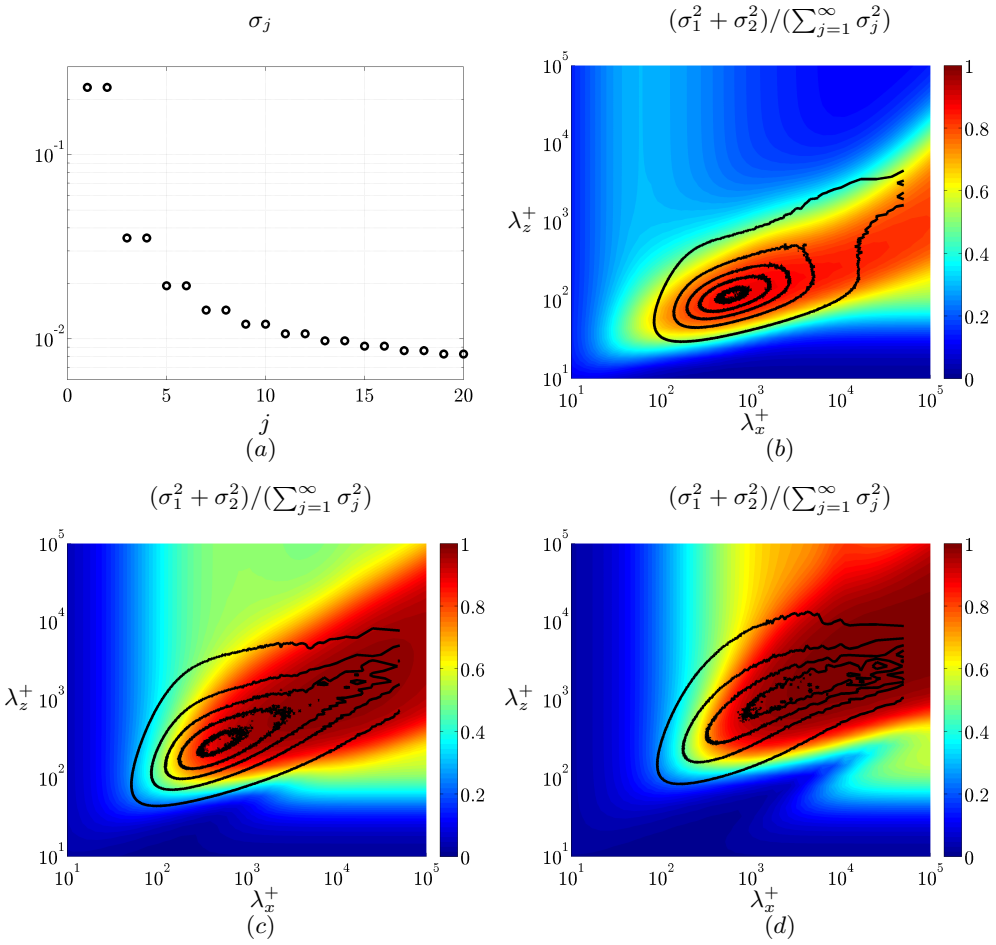

FIGURE 4. (a) The twenty largest singular values of H for $\lambda_x^+ = 700$, $\lambda_z^+ = 100$, $c = 10$, and $Re_\tau = 2003$. (b)-(d): The color plots show the energy that is contained in the largest two response modes relative to the total response for different streamwise and spanwise wavelengths and (b) $c = U(y^+ = 15)$; (c) $c = U(y^+ = 100)$; and (d) $c = U(y = 0.2)$. The black contours show the turbulent kinetic energy spectrum from the DNS of Hoyas & Jiménez (2006) at the corresponding critical wall-normal locations (b) $y^+ = 15$; (c) $y^+ = 100$; and (d) $y = 0.2$. The contours represent 10% to 90% of the maximum energy spectrum at each wall-normal location with increments of 20%.

the largest pair of singular values is approximately one order of magnitude larger than the other singular values.

The energetic contribution of the k-th direction $\hat{\boldsymbol{\psi}}_k$ to the total response in the model subject to broadband forcing in y with fixed λ_x, λ_z, and c is quantified by $\sigma_k^2/(\sum_{j=1}^{\infty}\sigma_j^2)$. Figures 4(b)-4(d) highlight the low-rank nature of H by showing that the first two principal response directions $\hat{\boldsymbol{\psi}}_1$ and $\hat{\boldsymbol{\psi}}_2$ contribute to more than 80% of the total response over a large range of wall-parallel wavelengths (red region) for wave speeds $c = U(y^+ = 15)$, $U(y^+ = 100)$, $U(y = 0.2)$, and $Re_\tau = 2003$. The relevance of studying the low-rank approximation of H is further emphasized by noting that the wavenumbers for which H is low-rank coincide with the most energetic wavenumbers from the DNS of Hoyas & Jiménez (2006) (contours) at the corresponding critical wall-normal locations.

2.4. *Rank-1 model subject to broadband forcing*

In the present study, we consider a rank-1 model by only keeping the most energetic forcing and response directions corresponding to σ_1 and show that significant understanding of the scaling of wall turbulence can be obtained using this simple model. This is motivated by the observation in § 2.3 that the operator H is essentially a directional amplifier. In other words, we expect to see the principal singular response of H in real turbulent flows provided that the principal forcing direction is present in the nonlinear forcing term; i.e. the gradient of the Reynolds-stresses. In order to use the least number of assumptions, we consider the case where the forcing $\hat{\mathbf{f}}$ equals the principal forcing direction $\hat{\boldsymbol{\phi}}_1$. Consequently, the forcing has unit energy for all wave parameters, meaning that it is broadband in κ_x, κ_z, and c.

It is well-known that the streamwise energy spectrum can be divided into regions that scale in inner and outer variables (see, for example, Morrison *et al.* 2004). Our objective is to explore the Reynolds number scaling of the streamwise energy density and predict the behavior of the streamwise turbulence intensity at high Re_τ. We focus on the streamwise velocity because it dominates the kinetic energy density in turbulent flows. Similarly, the principal singular responses of H that result in the largest energy amplification are dominated by their streamwise component. For the rank-1 model with broadband forcing, we define the premultiplied streamwise energy density of the principal response of H by

$$E_{uu}(y;\kappa_x,\kappa_z,c) \;=\; \kappa_x^2\kappa_z\left(\sigma_1(\kappa_x,\kappa_z,c)|u_1|(y;\kappa_x,\kappa_z,c)\right)^2, \tag{2.10}$$

such that the premultiplied one-dimensional energy densities and the energy intensity are obtained by integrating $E_{uu}(y;\kappa_x,\kappa_z,c)$ over the set of all wave parameters $\mathcal{S}$, e.g.

$$\begin{aligned} E_{uu}(y,c) &= \iint_{\mathcal{S}} E_{uu}(y;\kappa_x,\kappa_z,c)\,\mathrm{d}\log(\kappa_x)\,\mathrm{d}\log(\kappa_z), \\ E_{uu}(y) &= \iiint_{\mathcal{S}} E_{uu}(y;\kappa_x,\kappa_z,c)\,\mathrm{d}\log(\kappa_x)\,\mathrm{d}\log(\kappa_z)\,\mathrm{d}c, \end{aligned} \tag{2.11}$$

and $E_{uu}(y,\kappa_x)$ and $E_{uu}(y,\kappa_z)$ are determined similarly.

The above formulation of the energy density is used in § 3 to identify the contribution of confined subsets of wave parameters to the energy density. We establish that the energy density exhibits universal behavior with Re_τ for properly selected subsets of wave parameters. It is further shown that the emerging scales are consistent with those observed in experiments. In addition, the scales of energetically dominant waves roughly agree with the scales of dominant near-wall motions in real turbulent flows.

2.5. *Computational approach*

A pseudo-spectral method is used to discretize the differential operators in the wall-normal direction on a set of Chebyshev collocation points. This is implemented using the Matlab Differentiation Matrix Suite developed by Weideman & Reddy (2000). Table 1 summarizes the selected range of wave parameters and their respective resolution in numerical computations. It has been verified that the excluded wave parameters are not energetically important and therefore do not change the results of the present study.

An efficient randomized scheme developed by Halko *et al.* (2011) is utilized to compute the principal singular directions of H for different Reynolds numbers and wave parameters. The accuracy and computation time depend on the decay of the singular values; a faster decay results in high accuracy or equivalently less computation time to reach the same accuracy. In addition, if the singular values are not well separated, the problem of computing the associated singular functions is badly conditioned, meaning that it is

Re_τ	N_x	N_y	N_z	N_c	$\lambda^+_{x,\min}$	$\lambda_{x,\max}$	$y^+_{\min}$	$\lambda^+_{z,\min}$	$\lambda_{z,\max}$	U_{cl}
934	64	251	32	100	10	10^6	0.07	10	100	22.39
2003	64	251	32	100	10	5×10^5	0.15	10	50	24.02
3333	64	301	32	100	10	3×10^5	0.18	10	30	25.22
10000	64	401	32	100	10	10^5	0.3	10	10	27.81
30000	80	601	40	100	10	3.3×10^6	0.4	10	33	30.39

TABLE 1. Summary of the selected parameters in numerical computations at different Reynolds numbers. In the wall-normal direction, N_y Chebyshev collocation points is used with $y^+_{\min}$ denoting the closest point to the wall. In the streamwise and spanwise directions, N_x and N_z logarithmically spaced wavelengths are used between $\lambda^+_{\min}$ and $\lambda_{\max}$. In addition, N_c linearly spaced wave speeds are chosen between $c_{\min}=5$ and $c_{\max}=U_{cl}$.

hard for any method to determine them very accurately. In this study, the above scheme approximately halves the total computation time relative to Matlab's `svds` algorithm. This becomes increasingly important considering the three-dimensional wave parameter space that we need to explore and the large size of the discretized resolvent operator (twice the number of collocation points in y) at high Reynolds numbers. In addition, the randomized nature of this scheme enables its parallel implementation which makes it especially suitable for large-scale computations. Even though we have not used this feature in the present study, it may find use in designing turbulent flow control strategies, e.g. by means of spatially or temporally periodic actuations.

3. Reynolds number scaling

The formulation of § 2 facilitates analysis of the contribution of different wave parameters (κ_x,κ_z,c) to the streamwise energy density. For the rank-1 model with broadband forcing, the energy density of each wave is determined from the principal singular values and singular functions of the transfer function H; see (2.10). In this section, we identify three classes of wave parameters for which $E_{uu}(y;\kappa_x,\kappa_z,c)$ exhibits universal behavior with Re_τ. Each class is characterized by a unique range of wave speeds and a unique scaling of the wall-parallel wavelengths.

3.1. *Requirement for universal behavior*

We start by showing that a requirement for universal behavior is the wall-normal locality of the singular functions of H. This is done by examining the underlying operators in H, cf. (2.7):

$$
\begin{aligned}
A &= \begin{bmatrix} \Delta^{-1}\left((1/Re_\tau)\Delta^2 + \mathrm{i}\kappa_x\left(U''-U\Delta\right)\right) & 0 \\ -\mathrm{i}\kappa_z U' & (1/Re_\tau)\Delta - \mathrm{i}\kappa_x U \end{bmatrix},\\
C &= \frac{1}{\kappa^2}\begin{bmatrix} \mathrm{i}\kappa_x\partial_y & -\mathrm{i}\kappa_z \\ \kappa^2 & 0 \\ \mathrm{i}\kappa_z\partial_y & \mathrm{i}\kappa_x \end{bmatrix},\quad C^\dagger = \begin{bmatrix} -\mathrm{i}\kappa_x\Delta^{-1}\partial_y & \kappa^2\Delta^{-1} & -\mathrm{i}\kappa_z\Delta^{-1}\partial_y \\ \mathrm{i}\kappa_z & 0 & -\mathrm{i}\kappa_x \end{bmatrix},\\
R_A &= \begin{bmatrix} \Delta^{-1}\left(\mathrm{i}\kappa_x\left((U-c)\Delta - U''\right) - (1/Re_\tau)\Delta^2\right) & 0 \\ \mathrm{i}\kappa_z U' & \mathrm{i}\kappa_x(U-c) - (1/Re_\tau)\Delta \end{bmatrix}^{-1},
\end{aligned}
\tag{3.1}
$$

where $\Delta^2 = \partial_{yyyy} - 2\kappa^2\partial_{yy} + \kappa^4$, and prime denotes differentiation in y, e.g. $U'(y) = \mathrm{d}U/\mathrm{d}y$. We see that the difference between the turbulent mean velocity and the wave speed, $U(y) - c$, and its wall-normal derivatives, $U'(y)$ and $U''(y)$, appear as spatially-varying coefficients in H. Since the turbulent mean velocity scales differently with Re_τ in different wall-normal locations, only the singular functions that are sufficiently narrow in y have the potential to be universal. This is because such singular functions are purely affected by a certain part of the mean velocity that scales uniquely with Re_τ.

We next show that the singular functions corresponding to the energetically significant modes are in fact localized. Recent DNS (del Álamo & Jiménez 2009) and experiments (LeHew *et al.* 2011) have shown that the energetic contribution of structures with convection velocities less than $10u_\tau$ and larger than the centerline velocity $U_{cl} = U(y = 1)$ is negligible in real turbulent flows. This motivates defining a conservative subset of $\mathcal{S}$, denoted by $\mathcal{S}_e$, that includes all wall-parallel wavenumbers and the energetically important wave speeds

$$\mathcal{S}_e \;=\; \{(\kappa_x, \kappa_z, c) \;\;|\;\; 5 \le c \le U_{cl}\}\,. \tag{3.2}$$

Since a significant portion of the streamwise energy intensity is contained below $y^+ \approx 15$ (critical speed $c \approx 10$), we include the waves with $c < 10$ in $\mathcal{S}_e$ such that the principal singular functions peak for $y^+ < 15$.

Figure 5 shows the one-dimensional energy density as a function of wave speed $E_{uu}(y, c)$ for $Re_\tau = 30000$ and $\mathcal{S} = \mathcal{S}_e$. As evident from figure 5(a), the energy density for a fixed c is localized in a narrow wall-normal region; note that the colors are given in logarithmic scale. The localization is highlighted in figure 5(b) where $E_{uu}(y, c)$ is normalized by its maximum value over y for fixed values of c. We see that the largest energy amplification takes place in the vicinity of the critical wall-normal location where the turbulent mean velocity (thick white curve) equals the wave speed. McKeon & Sharma (2010) argued that emergence of critical layers is one of the three means of maximizing the Hilbert-Schmidt norm of H (sum of squares of the singular values), i.e. by locally minimizing the term $U(y) - c$ that appears in the resolvent operator R_A given in (3.1).

According to Taylor's frozen turbulence hypothesis (Taylor 1938), the flow structures in boundary layers propagate downstream with a speed close to the local mean velocity. Consistent with this hypothesis, figure 5(b) shows that among all the waves with arbitrary streamwise and spanwise wavelengths at the wall-normal location y, the ones with critical speed $c = U(y)$ are the most highly amplified. This provides strong evidence for the importance of critical layers in amplification of flow disturbances. In addition, figure 5(b) shows that the scatter in the energetic wave speeds increases as the peak of energy density approaches the wall. This agrees with the practical observation that Taylor's hypothesis yields inaccurate energy spectra close to the wall; see, for example, Kim & Hussain (1993); Monty & Chong (2009); del Álamo & Jiménez (2009); LeHew *et al.* (2011).

3.2. *Summary of the universal behavior with Re_τ*

We start by reviewing the universal behavior of the turbulent mean velocity. This is a prerequisite to studying the universality of the principal propagating waves since the latter holds for critical modes only, as discussed in § 3.1. In the commonly accepted picture (Coles 1956), the mean velocity is divided into inner, logarithmic, and outer regions

$$U \;=\; B(y^+) \,+\, (1/\kappa)\,\log(y^+) \,+\, (2\Pi/\kappa)\,W(y), \tag{3.3}$$

where B is the inner-scaled wall function, Π is the wake factor, W is the outer-scaled wake function, and the von Kármán's constant $\kappa = 0.426$ is taken to match the mean

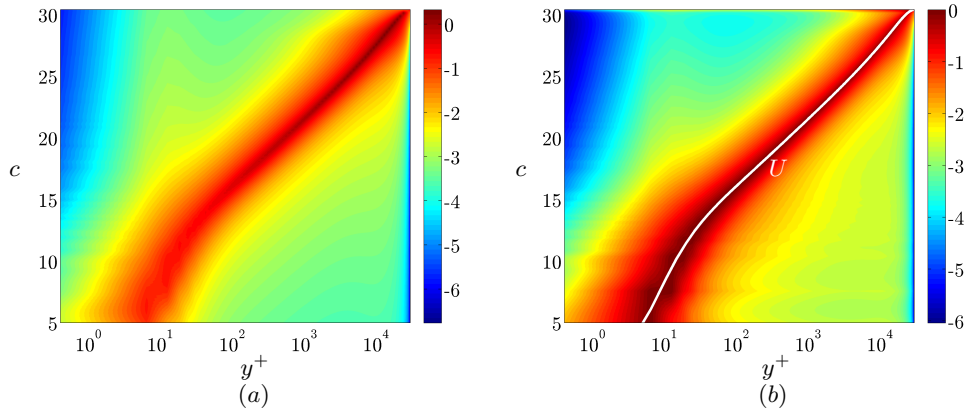

FIGURE 5. (a) The one-dimensional energy density $Re_\tau^{-2}E_{uu}(y,c)$ for $\mathcal{S}=\mathcal{S}_e$ and $Re_\tau=30000$; and (b) the energy density normalized by its maximum value over all y for fixed values of c. The colors are in logarithmic scale. The turbulent mean velocity is shown by the thick white curve in (b).

Region	Range of wave speeds	Wall-normal scale
Inner	$c \lesssim 16$	$y^+ \lesssim 100$
Logarithmic	$\lvert U_m - c\rvert \lesssim \frac{1}{2\kappa}\log\left(\frac{Re_{\tau,\min}}{50/0.2}\right)$	$\frac{50}{\sqrt{Re_{\tau,\min}}} \lesssim \sqrt{yy^+} \lesssim 0.2\sqrt{Re_{\tau,\min}}$
Outer	$0 \lesssim U_{cl} - c \lesssim 6$	$y \gtrsim 0.1$

TABLE 2. Summary of wave speeds and wall-normal intervals where $U-c$ is universal with Re_τ. The mean velocity is denoted by U_{cl} in the center plane and by U_m in the geometric mean of the logarithmic region. The smallest Reynolds number that is considered is denoted by $Re_{\tau,\min}$. See also the green regions in figures 6(b)-6(d)

Class	x-scale	y-scale	z-scale	t-scale	Subset of wave parameters
Inner	λ_x^+	y^+	λ_z^+	T_c^+	$\mathcal{S}_i: \; 5 \lesssim c \lesssim 16$
Outer-in-x	λ_x	$\sqrt{yy^+}$	$\sqrt{\lambda_z\lambda_z^+}$	T_m	$\mathcal{S}_{ox}: \begin{cases} \lvert U_m - c\rvert \lesssim \frac{1}{2\kappa}\log\left(\frac{Re_{\tau,\min}}{50/0.2}\right) \\ \lambda_x/\lambda_z \gtrsim \sqrt{10(Re_\tau/Re_{\tau,\min})} \end{cases}$
Outer-in-y	$\frac{\lambda_x}{Re_\tau}$	y	λ_z	$Re_\tau T_{cl}$	$\mathcal{S}_{oy}: \begin{cases} 0 \lesssim U_{cl} - c \lesssim 6 \\ \lambda_x/\lambda_z \gtrsim \sqrt{10}(Re_\tau/Re_{\tau,\min}) \end{cases}$

TABLE 3. Summary of universal wave parameters with Re_τ. See also figures 6(e)-6(g).

velocity given in (2.3) for high Re_τ. Consequently, $U-c$ is universal with Re_τ for certain intervals of wave speed and wall-normal scales; see table 2 and figures 6(a)-6(d).

Figure 6(b) shows that $U(y^+)-c$ is universal for $y^+ \lesssim 100$ and fixed $c \lesssim 16$ (inner region). As shown in figure 6(d), the function $U(y)-c$ is universal for $y \gtrsim 0.1$ and fixed defect wave speeds relative to the centerline $0 \lesssim U_{cl}-c \lesssim 6$, with $U_{cl}=U(y=1)$ (outer

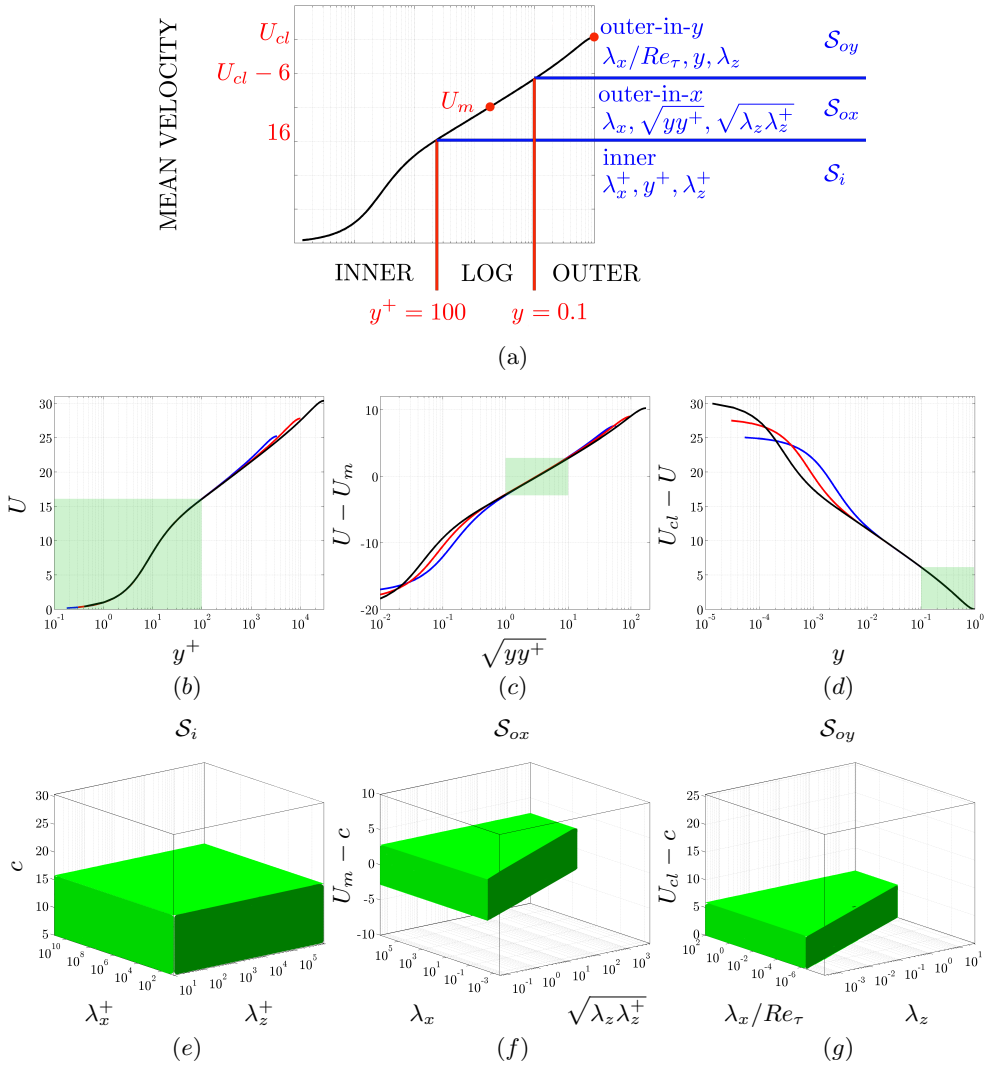

FIGURE 6. (a) Schematic of the the different regions of the mean velocity and the associated classes of Reynolds number scales that are induced on the propagating waves. (b) The turbulent mean velocity $U(y^+)$; (c) the defect velocity $U_{cl} - U(y)$ defined relative to the centerline; and (d) the defect velocity $U(\sqrt{yy^+}) - U_m$ defined relative to the geometric mean of the logarithmic region $y_m y_m^+ = 10$, for $Re_\tau = 3333$ (blue), $Re_\tau = 10000$ (red), and $Re_\tau = 30000$ (black). Notice that the shaded regions are invariant with Re_τ. (e)-(g): The classes of wave parameters $(\lambda_x, \lambda_z, c)$ that induce universal behavior with Re_τ on the low-rank approximation of H. (e) $\mathcal{S}_i$ induces the inner scale; (f) $\mathcal{S}_{oy}$ induces the outer-in-y scale; and (g) $\mathcal{S}_{ox}$ induces the outer-in-x scale. The classes $\mathcal{S}_{oy}$ and $\mathcal{S}_{ox}$ are obtained for $Re_\tau > Re_{\tau,\min} = 3333$.

region). The logarithmic region, taken for $y^+ \gtrsim 50$ and $y \lesssim 0.2$, bridges the gap between the inner and outer regions. Figure 6(c) illustrates that the function $U(\sqrt{yy^+}) - c$ is universal in the logarithmic region associated with the smallest Reynolds number $Re_{\tau,\min}$ that is considered, and for fixed defect wave speeds relative to the geometric mean of the logarithmic region $|U_m - c| \lesssim (1/2\kappa)\log(Re_{\tau,\min}/(50/0.2))$, with $U_m = U(\sqrt{yy^+} = \sqrt{10})$. For example, $Re_{\tau,\min} = 3333$ yields $|U_m - c| \lesssim 3$ and $1 \lesssim \sqrt{yy^+} \lesssim 10$, i.e. y is

Class	Subset	κ_x	$(\mathrm{d}/\mathrm{d}y)$	κ_z	$\omega_c, \omega_m, \omega_{cl}$	σ_1	u_1	E_{uu}
Inner	$\mathcal{S}_i$	Re_τ	Re_τ	Re_τ	Re_τ	Re_τ^{-1}	$Re_\tau^{1/2}$	Re_τ^2
Outer-in-x	$\mathcal{S}_{ox}$	1	$Re_\tau^{1/2}$	$Re_\tau^{1/2}$	1	$Re_\tau^{1/2}$	$Re_\tau^{1/4}$	Re_τ^2
Outer-in-y	$\mathcal{S}_{oy}$	Re_τ^{-1}	1	1	Re_τ^{-1}	Re_τ^2	1	Re_τ^2

TABLE 4. Summary of the growth/decay rates with Re_τ of the wall-parallel wavenumbers, the wall-normal derivative, the convective frequency, the principal singular value and the principal streamwise singular function of H, and the premultiplied three-dimensional streamwise energy density for the three classes of universal waves with Re_τ.

approximately within a factor of $\sqrt{10}$ from the geometric mean of the logarithmic region. We note that the latter scale in the logarithmic region also emerges from the resolvent operator such that an outer scaling is imposed on the streamwise wavelength.

Associated with each region of the mean velocity, there is a class of wave parameters for which the low-rank approximation of H exhibits universal behavior with Re_τ; see tables 3 and 4 for a summary. As illustrated in figures 6(a) and 6(e)-6(g), these classes are primarily distinguished by the wave speed. The principal singular functions inherit their wall-normal length scale from the turbulent mean velocity at the critical layer, and their streamwise and spanwise length scales from the resolvent. In addition, the magnitude of the singular values and singular functions scale uniquely with Re_τ in each class of wave parameters, which induces unique scales on the premultiplied streamwise energy density $E_{uu}(y;\kappa_x,\kappa_z,c)$. Next, we separately discuss each class and refer the reader to Appendix A for detailed derivation of the scales.

3.2.1. *The inner class $\mathcal{S}_i$*

For wave speeds in the inner region of the turbulent mean velocity, universality of H requires constant λ_x^+, y^+, λ_z^+, and c; cf. table 3 and figure 6(e). As a result, the time $T_c = \lambda_x/c$ over which the wave convects downstream for one wavelength relative to the wall reduces with Re_τ and the convective frequency $\omega_c = 2\pi/T_c$ increases with Re_τ. In other words, a truly inner scale is induced on the length, height, width, and convective time of the waves that correspond to the principal singular functions. Therefore, the wall-normal support of the singular functions in outer units linearly decreases with Re_τ, and the unit energy constraint on the singular functions requires that the magnitude of the singular functions increase with $Re_\tau^{1/2}$. The number of these waves per unit wall-parallel area and time increases with Re_τ^3 as their length, width, and convective time decrease with Re_τ. Since the singular values of H linearly decrease with Re_τ, the overall result is that $E_{uu}(y;\kappa_x,\kappa_z,c)$ increases with Re_τ^2; cf. table 4.

3.2.2. *The outer-in-x class $\mathcal{S}_{ox}$*

For wave speeds in the logarithmic region of the turbulent mean velocity, universality of H requires constant λ_x, y^+y, $\lambda_z^+\lambda_z$, and $U_m - c$, such that the aspect ratio constraint $\lambda_x/\lambda_z \gtrsim \sqrt{10Re_\tau/Re_{\tau,\min}}$ is satisfied; cf. table 3 and figure 6(f). As a result, the time $T_m = \lambda_x/|U_m - c|$ over which the wave convects away for one wavelength relative to an observer with speed U_m remains independent of Re_τ and same does the convective frequency $\omega_m = 2\pi/T_m$. These waves have the same scales as the structures in the meso-layer; see, for example, Long & Chen (1981); Afzal (1984); Sreenivasan & Sahay (1997); Wei *et al.* (2005). We see that the aspect ratio λ_x/λ_z of the universal waves increases as $Re_\tau^{1/2}$. This explains why universality for this class holds for the waves with aspect

ratios larger than a threshold: As the aspect ratio of the singular modes increases with Reynolds number, the Laplacian operator in the resolvent becomes independent of κ_x. Therefore, the necessary condition for the Laplacian to be universal with Re_τ is that κ_z dominates κ_x even for the smallest Reynolds number $Re_{\tau,\min}$ that is considered. This poses the above-mentioned aspect ratio constraint on the universal waves. The magnitude of the corresponding singular functions increases with $Re_\tau^{1/4}$ because of the unit energy constraint. The number of waves per unit area and time increases with $Re_\tau^{1/2}$. In addition, the principal singular values of the waves in $\mathcal{S}_{ox}$ increase with $Re_\tau^{1/2}$. The above scales result in growth of $E_{uu}(y;\kappa_x,\kappa_z,c)$ with Re_τ^2; cf. table 4.

3.2.3. *The outer-in-y class $\mathcal{S}_{oy}$*

For wave speeds close to the centerline, universality of H requires constant λ_x/Re_τ, y, λ_z, and $U_{cl}-c$, such that the aspect ratio constraint $\lambda_x/\lambda_z \gtrsim \sqrt{10}Re_\tau/Re_{\tau,\min}$ is satisfied; cf. table 3 and figure 6(g). As a result, the time $T_{cl}=\lambda_x/(U_{cl}-c)$ over which the wave convects upstream for one wavelength relative to an observer with speed U_{cl} increases with Re_τ and the convective frequency $\omega_{cl}=2\pi/T_{cl}$ decreases with Re_τ. The aspect ratio constraint follows from similar arguments to those discussed for the outer-in-x class. The magnitude of singular functions is independent of Re_τ since the singular functions scale with outer units in the wall-normal direction. The number of waves per unit area and time decreases with Re_τ^2 since their length and convective time increase with Re_τ. The singular values increase with Re_τ^2 and the overall result is that the energy density $E_{uu}(y;\kappa_x,\kappa_z,c)$ increases with Re_τ^2; cf. table 4.

The waves in the outer-in-y class asymptotically approach the streamwise constant fluctuations, i.e. $\kappa_x=0$, as Re_τ increases. These infinitely long fluctuations exhibit the largest linear transient growth in response to initial perturbations in laminar (Gustavsson 1991; Butler & Farrell 1992; Reddy & Henningson 1993) and turbulent (Butler & Farrell 1993; del Álamo & Jiménez 2006; Pujals *et al.* 2009) flows. In addition, they are the most highly amplified by the linear dynamics in laminar (Farrell & Ioannou 1993*b*; Bamieh & Dahleh 2001; Jovanović & Bamieh 2005) and turbulent (Hwang & Cossu 2010) flows subject to stochastic disturbances.

The effect of Reynolds number on the streamwise constant fluctuations has been studied in laminar flows. For example, Gustavsson (1991) showed that the peak of linear transient growth scales with the square of centerline Reynolds number $R_{cl}=U_{cl}h/\nu$. For the flow subject to harmonic disturbances, Jovanović & Bamieh (2005) showed that the singular values of H increase as R_{cl}^2 when the temporal frequency ω linearly decreases with R_{cl}. No other scales for the singular values were found since the laminar mean velocity $U/U_{cl}=2y-y^2$ is universal with Reynolds number throughout the channel. Our study shows that the singular values in the turbulent flow increase quadratically with Re_τ for the waves with defect speeds, $U_{cl}-c \lesssim 6$, and streamwise wavelengths that linearly increase with Re_τ, i.e. $\lambda_x \gtrsim \sqrt{10}\,\lambda_z Re_\tau/Re_{\tau,\min}$; cf. table 4.

3.3. *Universality of the streamwise energy density*

We compute the streamwise energy density of the rank-1 model with broadband forcing and illustrate its universal behavior with Re_τ. These computations build the basis for prediction of the streamwise energy intensity at the technologically relevant values of Re_τ in § 4. Because of the unique scales in the inner, outer-in-x, and outer-in-y classes of wave parameters, we distinguish the corresponding intervals of wave speeds by expanding

the premultiplied energy density into the following three integrals:

$$\begin{aligned} E_{uu}(y,\kappa_x,\kappa_z) &= \int_5^{16} E_{uu}(y,\kappa_x,\kappa_z,c)\,\mathrm{d}c + \\ &= \int_{16}^{U_{cl}-6} E_{uu}(y,\kappa_x,\kappa_z,c)\,\mathrm{d}c + \int_{U_{cl}-6}^{U_{cl}} E_{uu}(y,\kappa_x,\kappa_z,c)\,\mathrm{d}c. \end{aligned} \tag{3.4}$$

Similar expansions can be written for $E_{uu}(y,\kappa_x)$, $E_{uu}(y,\kappa_z)$, and $E_{uu}(y)$. Notice that in spite of the different behavior of singular values and singular functions, the energy density increases with Re_τ^2 in all three classes of wave parameters. Figure 7 shows the premultiplied one-dimensional energy densities and the energy intensity confined to each class of wave parameters and normalized by Re_τ^2. The same contour levels are used for all Reynolds numbers, $Re_\tau = 3333$ (blue), 10000 (red), and 30000 (black), in figures 7(a)-7(f). Notice that confining the wavenumbers to $\mathcal{S}_i$, $\mathcal{S}_{ox}$, and $\mathcal{S}_{oy}$ yields a universal energy density as summarized in tables 3 and 4.

The inner peak of streamwise energy density in the rank-1 model with broadband forcing occurs at $y^+ \approx 11$, $\lambda_x^+ \approx 184$, and $\lambda_z^+ \approx 44$; see figures 7(a) and 7(d). The location of the above wall-normal peak represents an integral effect over all wave parameters in $\mathcal{S}_i$ and corresponds to the critical speed $c \approx 8.5$. The inner peak is comparable with the location, length, and spacing of the most energetic structures associated with the near-wall cycle, i.e. $y^+ \approx 15$, $\lambda_x^+ \approx 700-1000$, and $\lambda_z^+ \approx 100$ (see, for example, Hoyas & Jiménez 2006). The outer-in-x peak takes place at $\sqrt{yy^+} \approx 5.2-5.8$ (corresponding to critical speed $c \approx U_m$), $\lambda_x \approx 12-16$, and $\sqrt{\lambda_z\lambda_z^+} \approx 20$; see figures 7(b) and 7(e). It has the same scaling as the VLSMs and its location is comparable with the most energetic VLSMs located at $\sqrt{yy^+} \approx 3.9$ and $\lambda_x \approx 6$ in boundary layers (see, for example, Marusic *et al.* 2010*a*) and at $\lambda_x \approx 12-20$ in pipes and channels (see, for example, Monty *et al.* 2009). These agreements are striking considering the simplicity of the rank-1 model subject to broadband forcing. Figures 7(c) and 7(f) show that the outer-in-y peak takes place at $y \approx 0.45$ (corresponding to critical defect speed $U_{cl}-c \approx 2$) for $\lambda_x/Re_\tau \approx 0.1$, and $\lambda_z \approx 2$. This peak points to much longer structures relative to the LSM structures observed in experiments, i.e. $\lambda_x \approx 3$ (see, for example in boundary layers, Adrian *et al.* 2000). The same length scales are reported for channels and pipes (see, for example, Guala *et al.* 2006; Monty *et al.* 2009).

The one-dimensional energy densities can be integrated in the remaining wall-parallel direction to obtain the streamwise energy intensity $E_{uu}(y)$ for the rank-1 model with broadband forcing. The dashed curves in figures 7(g)-7(i) are the energy intensities normalized by Re_τ^2 obtained by confining the wave parameters to $\mathcal{S}_i$, $\mathcal{S}_{ox}$, and $\mathcal{S}_{oy}$, respectively. As expected, the energy intensities are independent of Reynolds number when confined to the universal classes of wave parameters. The solid curves are obtained by integrating the energy density over all wavenumbers and wave speeds $5 \le c \le U_{cl}$, i.e. by confining the wave parameters to $\mathcal{S}_e$. These figures highlight the selection of two local peaks by the linear amplification mechanism where the inner and outer-in-y peaks dominate the outer-in-x peak. The inner peak takes place close to the inner peak of the streamwise intensity in real turbulent flows. While the energy intensity of real flows exhibits outer scales near the center of the channel, there is no strong evidence for presence of an outer-in-y peak even for high Re_τ.

As evident from figure 7(g), the universal inner waves contribute to more than 96% of the total energy intensity for $y^+ < 20$ for all Reynolds numbers. On the other hand, figure 7(i) shows that the universal outer-in-y waves capture a smaller amount of the total intensity for $y = 0.45$ as Re_τ increases; 95% for $Re_\tau = 3333$ vs. 86% for $Re_\tau = 30000$.

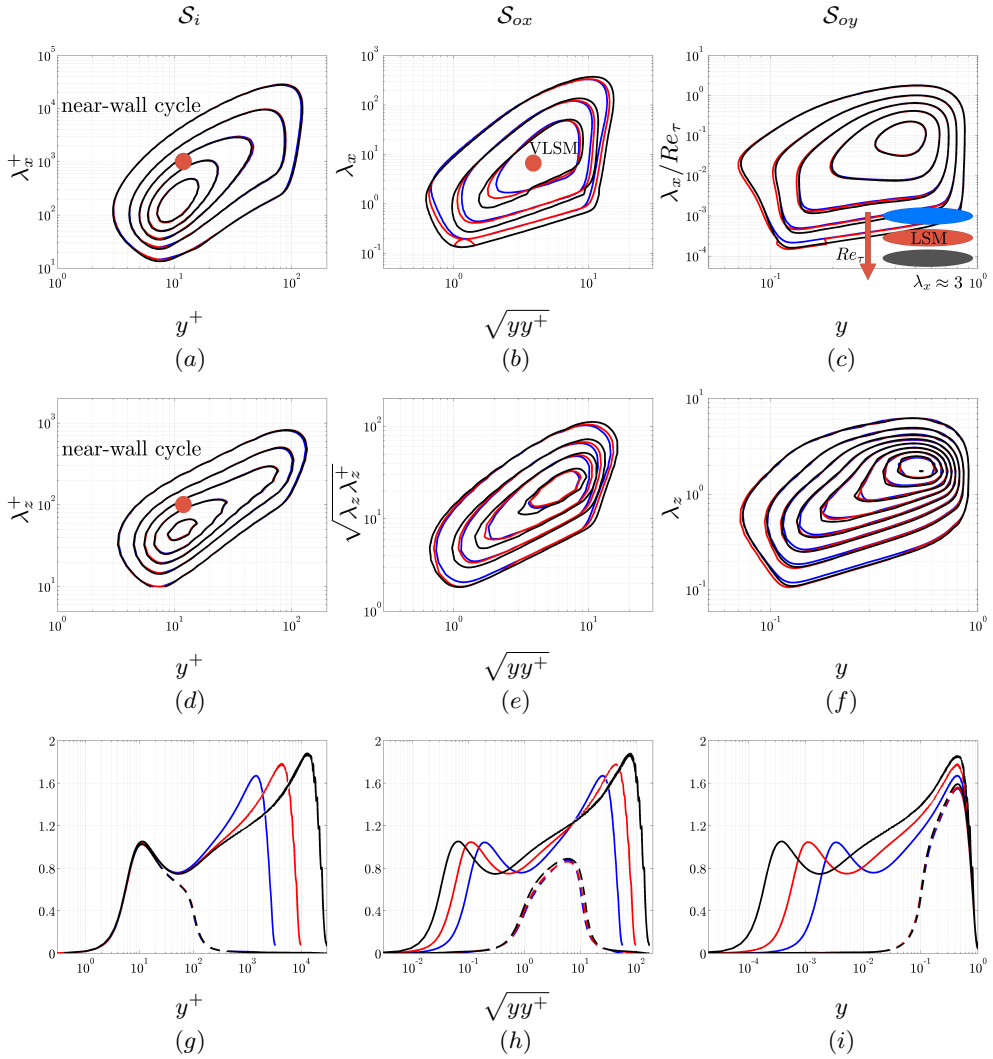

FIGURE 7. The premultiplied one-dimensional streamwise energy density $Re_\tau^{-2}\,E_{uu}(y,\lambda_x)$ in (a)-(c); and $Re_\tau^{-2}\,E_{uu}(y,\lambda_z)$ in (d)-(e); and the streamwise energy intensity $Re_\tau^{-2}\,E_{uu}(y)$, dashed curves in (g)-(i) for the rank-1 model with broadband forcing. The wave parameters are confined to $\mathcal{S}=\mathcal{S}_i$ in (a), (d), (g); $\mathcal{S}=\mathcal{S}_{ox}$ in (b), (e), (h); and $\mathcal{S}=\mathcal{S}_{oy}$ in (c), (f), (i). The Reynolds numbers are $Re_\tau=3333$ (blue), $Re_\tau=10000$ (red), and $Re_\tau=30000$ (black). The contour levels decrease by 0.05 from their maximum value of 0.25 (a); 0.15 (b); and 0.25 (c), and by 0.1 from their maximum value of 0.5 (d); 0.4 (e); and 0.8 (f). The solid curves in (g)-(i) are obtained by confining the wave parameters to $\mathcal{S}=\mathcal{S}_e$.

This is because the aspect ratio constraint in $\mathcal{S}_{oy}$ excludes more wavenumbers from $\mathcal{S}_e$ as Re_τ increases. The excluded waves are not universal with Re_τ and their contribution to the energy intensity is not completely negligible. A similar reasoning explains why the universal outer-in-x scale captures 82% of the total energy intensity at $\sqrt{yy^+}=\sqrt{10}$ for $Re_\tau=3333$ vs. 72% for $Re_\tau=30000$; cf. figure 7(h).

At the end of this section, we recall that the streamwise energy densities and intensities thus far were obtained for the model with broadband forcing in λ_x, λ_z, and c. In § 4, we consider a non-broadband forcing by introducing an optimally shaped energy density.

4. Predicting the streamwise energy intensity

In this section, we introduce a model for predicting the energy intensity of real turbulent flows by considering a non-broadband forcing in wave speed. This is done by incorporating a positive weight function $W(c)$ that amplifies or attenuates the energy density $E_{uu}(y,c)$ of the rank-1 model with broadband forcing. Even though $W(c)$ differs from a true forcing spectrum (that also depends on the wall-parallel wavelengths), it provides the model with sufficient degrees of freedom for predicting the energy intensity. In addition, since each wave speed is associated with a certain class of wavelengths, $W(c)$ affects different classes of wavelengths as the wave speed changes.

First, we show that $W(c)$ can be optimally shaped such that the model-based streamwise energy intensity,

$$E_{uu,W}(y) \;=\; \int_2^{U_{cl}} W(c)\, E_{uu}(y,c)\, \mathrm{d}c, \tag{4.1}$$

matches the intensity of real flows at low Reynolds numbers. Then, we derive similarity laws to approximate the optimal weight functions at high values of Re_τ. These weight functions in conjunction with the energy density of the rank-1 model with broadband forcing enable prediction of the streamwise energy intensity at technologically relevant Reynolds numbers.

4.1. *Optimal weights for small Reynolds numbers*

The weight function $W(c)$ is determined by minimizing the deviation between $E_{uu,W}(y)$ in (4.1) and the streamwise energy intensity obtained from DNS, $E_{uu,\mathrm{DNS}}(y)$, in the interval $y^+ \geq 1$ and $y \leq 0.8$. We do not enforce matching for $y \geq 0.8$ since it requires significantly large values of $W(c)$ for wave speeds close to U_{cl}. This is because $E_{uu}(y,c)$ is considerably smaller and more localized near the centerline compared to other locations and results in sensitivity of $W(c)$; see, for example, figure 5(a) for $y^+ > 24000$ corresponding to $y > 0.8$ for $Re_\tau = 30000$. Note that the main amplification mechanisms for waves with speeds close to U_{cl} is criticality of the singular functions since the non-normality effect is small as the mean shear approaches zero. This results in small gains and singular functions that are localized in the wall-normal direction.

Since $E_{uu}(y,c)$ scales with Re_τ^2 (cf. table 4) while $E_{uu,\mathrm{DNS}}(y)$ does not, we find the normalized weight function $\overline{W}(c) = Re_\tau^2\, W(c)$ that solves the following optimization problem

$$\begin{aligned} &\text{minimize:} \quad \frac{\|E_{uu,\mathrm{DNS}}(y) \,-\, E_{uu,W}(y)\|_e^2}{\|E_{uu,\mathrm{DNS}}(y)\|_e^2} \,+\, \gamma_w\, \|\overline{W}(c)\|_w^2, \\ &\text{subject to:} \quad \overline{W}(c) > 0,\; 2 \leq c \leq U_{cl}. \end{aligned} \tag{4.2}$$

Here, $\|g(y)\|_e$ is defined as (note integration in $\log y^+$)

$$\|g(y)\|_e^2 \;=\; \int_0^{\log(0.8Re_\tau)} g^2(\log y^+)\, \mathrm{d}\log y^+,$$

to equally penalize the deviation of energy intensities near the inner peak as well as in the channel core. The second term in the objective function,

$$\|\overline{W}(c)\|_w^2 \;=\; \frac{1}{U_{cl}-2}\int_2^{U_{cl}} \overline{W}^2(c)\, \mathrm{d}c,$$

provides the weight function with smoothness by penalizing the magnitude of $\overline{W}$, and $\gamma_w \geq 0$ controls the importance of smoothness relative to matching the model-based and DNS-based energy intensities.

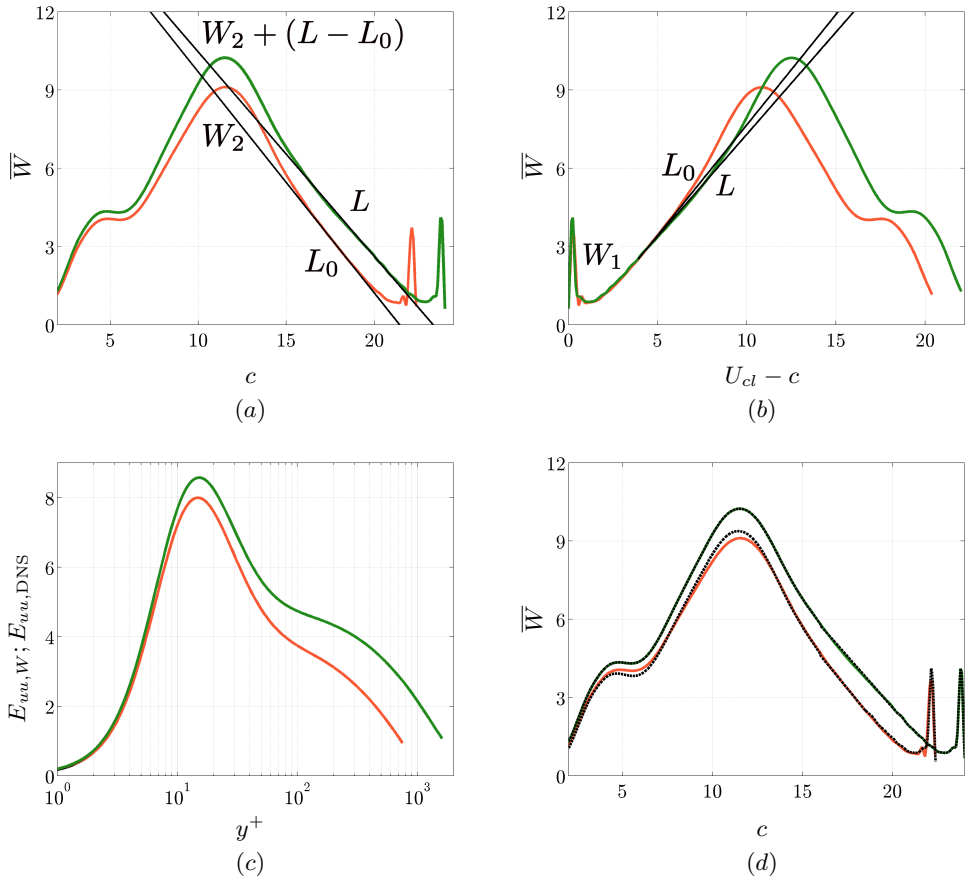

FIGURE 8. (a)-(b): The optimal weight functions $\overline{W}$ as a function of c in (a) and $U_{cl} - c$ in (b) for $Re_\tau = 934$ (orange) and 2003 (green). The tangent lines, L, to $\overline{W}(U_{cl} - c)$ at $U_{cl} - c = 3.9$ for each Re_τ are shown in black. (c) The model-based streamwise energy intensity $E_{uu,\mathrm{W}}(y^+)$ for $Re_\tau = 934$ (orange) and 2003 (green) and the DNS-based intensity $E_{uu,\mathrm{DNS}}(y^+)$ (black) are optimally matched by solving (4.2) for each Re_τ. The respective curves lie on the top of each other. (d) The optimal weight functions $\overline{W}$ for $Re_\tau = 934$ (orange) and 2003 (green) are compared with the weight functions obtained using the similarity law (4.4) (black dots).

The optimization problem (4.2) is solved using CVX, a package for specifying and solving convex programs in Matlab (CVX Research, Inc. 2012; Grant & Boyd 2008). We find the optimal weights for the largest Reynolds numbers that are simulated to date using DNS, i.e. $Re_\tau = 934$ (del Álamo *et al.* 2004) and $Re_\tau = 2003$ (Hoyas & Jiménez 2006). Even though these are orders of magnitude smaller than the Reynolds numbers for which we predict the energy intensity in § 4.2, they are free of measurement errors and useful for finding the optimal weights. We choose $\gamma_w = 0.2$ to strike a balance between matching error $\|E_{uu,\mathrm{DNS}}(y) - E_{uu,W}(y)\|_e^2$ and smoothness of $\overline{W}(c)$. The optimization problem is robust with respect to the choice of γ_w. For example, changing γ_w by a factor of two has negligible effect on the matching error and the optimal weights for $7 \lesssim c \lesssim U_{cl} - 2$ while slightly modifying $\overline{W}(c)$ elsewhere.

Figures 8(a) and 8(b) show the optimal weights as a function of c and $U_{cl} - c$ for $Re_\tau = 934$ and 2003. These weight functions match $E_{uu,\mathrm{DNS}}$ and $E_{uu,W}$ with a relative

error of approximately 0.2%; see figure 8(c). As expected, $\overline{W}$ is qualitatively similar for $c \lesssim 16$ and $U_{cl} - c \lesssim 6$ since both the model-based and DNS-based intensities exhibit inner and outer scaling in the respective regions. Figure 8(b) shows that $\overline{W}(U_{cl} - c)$ approximately coincides for $Re_\tau = 934$ and 2003 for $U_{cl} - c \leq 3.9$. We denote this universal function by $W_1(U_{cl} - c)$. For simplicity, the weights are approximated by linear functions in the logarithmic region for $16 \leq c \leq U_{cl} - 3.9$. These lines are denoted by L (black) and intersect for $L(c = -2) = 19.88$ and $L(U_{cl} - c = 3.9) = 2.54$. This gives an analytical expression for L as a function of wave speed and Reynolds number since U_{cl} varies with Re_τ

$$L(c; Re_\tau) \;=\; 2.54 \,+\, 17.34 \left(\frac{U_{cl} - c - 3.9}{U_{cl} - 1.89} \right). \tag{4.3}$$

As the Reynolds number increases, $\overline{W}(c)$ is shifted upward for $c \leq 16$ by the kick that it receives from the logarithmic region. This is expected since the DNS-based energy intensity increases with Re_τ in the inner region while $E_{uu}(y^+, c)$ remains constant. More discussion about the relationship between the weights in the logarithmic and inner regions are provided in § 4.2. Motivated by these observations, we formulate a similarity law for the weight function:

$$\overline{W}(c; Re_\tau) \;=\; \begin{cases} W_2(c) \,+\, \big(L(c; Re_\tau) - L_0(c)\big), & 2 \leq c \leq 16, \\ L(c; Re_\tau), & 16 < c < U_{cl} - 3.9, \\ W_1(U_{cl} - c), & U_{cl} - 3.9 \leq c \leq U_{cl}, \end{cases} \tag{4.4}$$

that consists of three segments: A universal outer segment represented by $W_1(U_{cl} - c)$ for $U_{cl} - 3.9 \leq c \leq U_{cl}$; a Reynolds number dependent linear segment $L(c; Re_\tau)$ that is analytically determined by (4.3); and an inner segment composed of a universal function $W_2(c)$ for $2 \leq c \leq 16$ superposed by a linear function $L(c; Re_\tau) - L_0(c)$ where $L_0(c) = L(c; Re_\tau = 934)$. Figure 8(d) shows that the optimal weights computed by solving (4.2) are well-captured by the weights formulated using the similarity law (4.4).

4.2. *Predictions at high Reynolds numbers*

The similarity law in (4.3)-(4.4) is used to predict the weight functions, and consequently, the streamwise energy intensity at high Re_τ using (4.1). Figure 9 shows the predicted weights and energy intensities for $Re_\tau = 934$, 2003, 3333, 10000, and 30000. As evident from figures 9(c) and 9(d), the model-based predictions are consistent with the experiments of channel flows (Monty 2005) up to $Re_\tau = 4000$ and boundary layers (Kunkel & Marusic 2006) up to $Re_\tau = 23013$. A logarithmic dependence of the energy intensity on the distance from the wall is predicted in the logarithmic region of the mean velocity which is consistent with recent experiments (Hultmark *et al.* 2012; Marusic *et al.* 2013) and predictions of the attached eddy hypothesis (see, for example, Perry & Chong 1982). The predicted intensity for $Re_\tau = 3333$ lies between the experimental data for channel flows at $Re_\tau = 3165$ and 4000 (Monty 2005). The experimental measurements are not accurate near the wall as they suffer from spatial resolution issues (see, for example, Hutchins *et al.* 2009). Figure 9(d) shows that the predicted values of the inner peak are consistent with the boundary layer measurements that are corrected (Kunkel & Marusic 2006) based on the attached eddy hypothesis. On the other hand, our predictions of the energy intensity in channel flow are larger than the data in boundary layers close to the outer peak in the logarithmic region. This is expected since recent experiments have shown that the large structures are more energetic in internal flows such as channels and pipes compared to boundary layers (see, for example, Monty *et al.* 2009). This difference

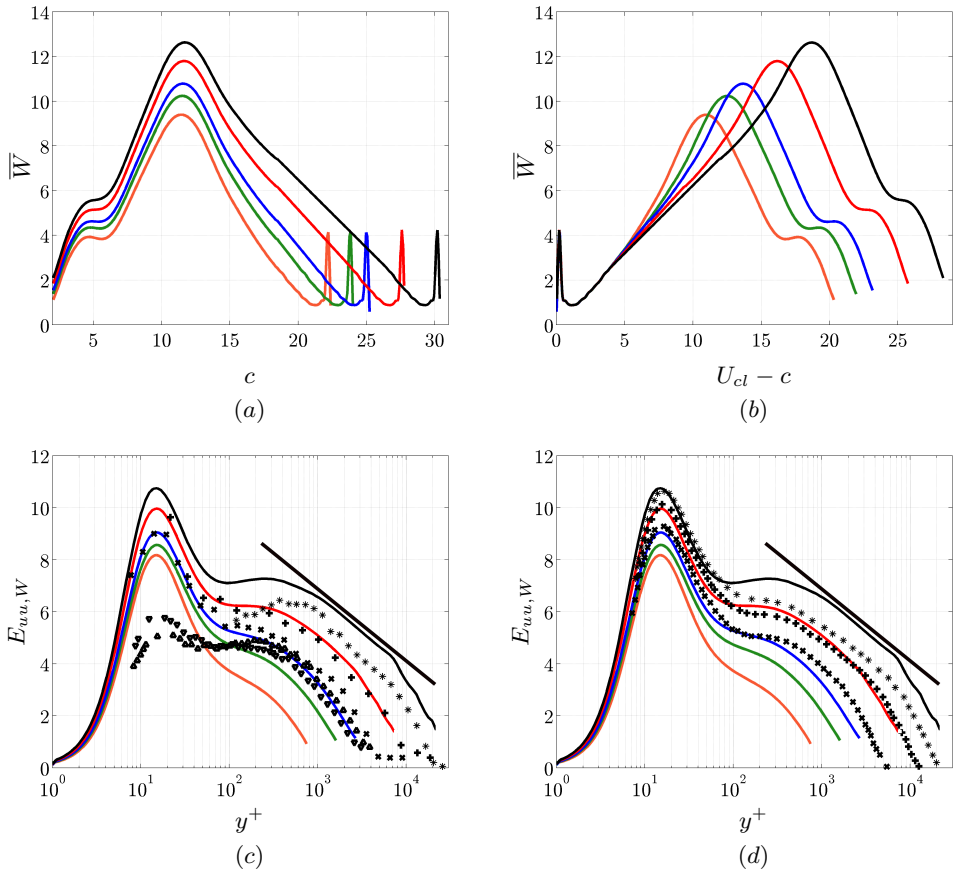

FIGURE 9. (a)-(b): The optimal weight functions $\overline{W}$ obtained using the similarity law (4.4) as a function of c in (a) and $U_{cl}-c$ in (b). (c)-(d): The corresponding model-based streamwise energy intensity $E_{uu,\mathrm{W}}(y^+)$ for $Re_\tau = 934$ (orange), 2003 (green), 3333 (blue), 10000 (red), and 30000 (black). The symbols in (c) are experimental data from channel flows (Monty 2005) $Re_\tau = 3165$; $\triangledown$ and 4000; $\triangle$, and from boundary layers (Kunkel & Marusic 2006) for $Re_\tau = 5813$; $\times$, 13490; $+$, 23013; $\star$. The symbols in (d) are the corrected (Kunkel & Marusic 2006) data in the inner region using attached eddy hypothesis. The lines show logarithmic scaling.

was attributed to the observations suggesting that the VLSMs are longer in internal flows than in boundary layers.

Obtaining the results of figure 9 requires computation of the streamwise energy density of the rank-1 model with broadband forcing at the respective values of Re_τ. Alternatively, the universal behavior of $E_{uu}(y;\kappa_x,\kappa_z,c)$ can be used to avoid these computations. In the present study, we employ the universality (invariance with Re_τ) of $E_{uu}(y;\kappa_x,\kappa_z,c)$ for $\mathcal{S}_i$ to predict the inner peak of the streamwise intensity at arbitrary high Re_τ. Expanding the weighted energy density according to the wave speed and substituting for the weight

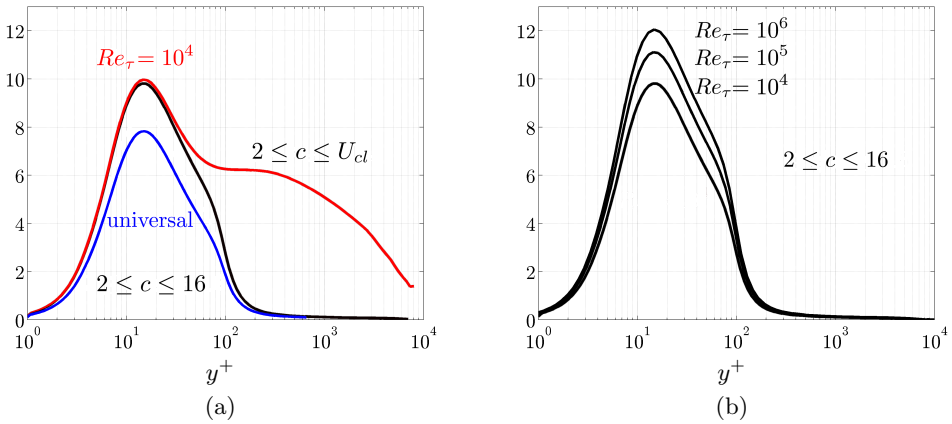

FIGURE 10. (a) The red curve is the model-based energy intensity $E_{uu,W}(y)$ for $Re_\tau = 10^4$. The blue curve is the contribution from the universal function in (4.5), and the black curve is the contribution from the inner class of wave parameters $\mathcal{S}_i$. (b) The contribution to the energy intensity from the inner class of wave parameters for $Re_\tau = 10^4$, 10^5, and 10^6.

function using the similarity law (4.4) yields

$$E_{uu,W}(y) = \int_2^{16} \underbrace{W_2(c)\big(Re_\tau^{-2}E_{uu}(y,c)\big)}_{\text{universal}} \left(1 + \frac{L(c;Re_\tau) - L_0(c)}{W_2(c)}\right) \mathrm{d}c + \int_{16}^{U_{cl}-3.9} L(c;Re_\tau)\left(Re_\tau^{-2}E_{uu}(y,c)\right)\mathrm{d}c + \int_{U_{cl}-3.9}^{U_{cl}} W_1(c)\left(Re_\tau^{-2}E_{uu}(y,c)\right)\mathrm{d}c. \tag{4.5}$$

The first integral, corresponding to the inner class of wave parameters $\mathcal{S}_i$, contains a universal function multiplied by a coefficient $L(c;Re_\tau)$ that also appears in the second integral for the faster and larger waves in the logarithmic region. It represents the contribution from the inner class of wave parameters that are coupled with and amplified by the large scales in the logarithmic region. This is similar to the model that Marusic *et al.* (2010*b*) proposed to capture the influence of the large scales u_L (close to the geometric mean of the logarithmic region) on the small scales u_S close to the inner peak of the energy intensity

$$u_S = u^*(1 + \beta\, u_L) + \alpha\, u_L. \tag{4.6}$$

For the purpose of the present study, (4.6) implies that the small structures are determined by a universal inner-scaled function u^* multiplied by a coefficient $1 + \beta\, u_L$ that increases with the energy of the large structures. Physically, the first term in (4.6) describes the amplitude modulation of small scales by the large scales and the second term represents the direct superimposition of the large scales on the inner-scaled near-wall peak (Marusic *et al.* 2010*b*).

The blue curve in figure 10(a) shows the contribution of the universal function in (4.5) to the energy intensity. This is equal to the contribution of the inner class of wave parameters to the energy intensity for $Re_\tau = 934$, i.e. for $L = L_0$. In other words, the inner class of wave parameters is not influenced by the large scales in the logarithmic region for $Re_\tau = 934$. This is expected since $Re_\tau \approx 1000$ is the smallest Reynolds number where the purely inner and outer scales are separated by a logarithmic region. The black

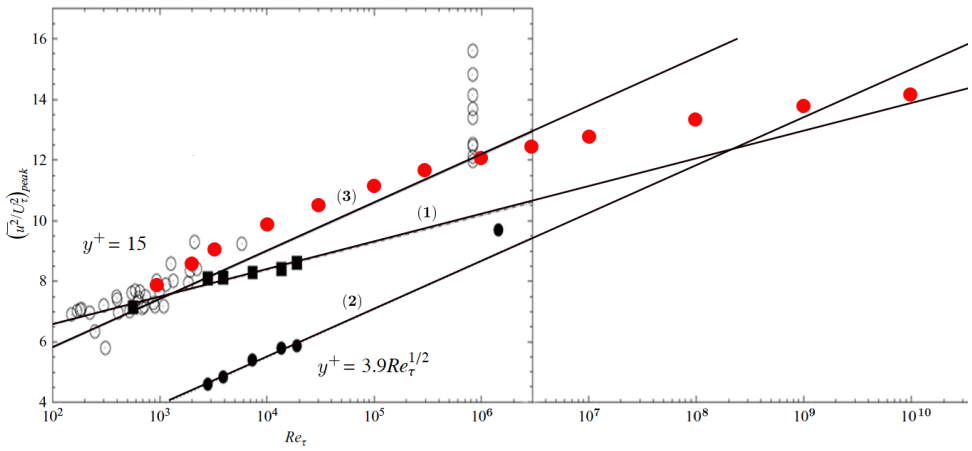

FIGURE 11. Variation of the inner ($y^+ = 15$) and outer ($y^+ = 3.9Re_\tau^{1/2}$) peaks of the streamwise energy intensity with Reynolds number. The figure is adapted from Marusic *et al.* (2010*a*). The black symbols are experimental and simulation data from channels and boundary layers. The red symbols are the predicted inner peak intensities obtained from the present model for turbulent channels.

curve shows the contribution of the first integral in (4.5) to the streamwise intensity for $Re_\tau = 10^4$. Notice that the large scales from the logarithmic region increase the inner peak by amplifying the universal function through the coefficient $1+(L-L_0)/W_2$. The red curve is the total intensity obtained by integrating the contribution of all wave parameters $\mathcal{S}_e$. The inner peak is captured by the first integral and the direct superimposition of the large scales on the inner peak is negligible. Therefore, the first integral readily yields the behavior of the streamwise intensity near the inner peak. For example, figure 10(b) illustrates how the more energetic large scales at $Re_\tau = 10^5$ and 10^6 further increase the inner peak relative to $Re_\tau = 10^4$ by amplifying the universal function W_2.

The red circles in figure 11 show the predicted value of the inner peak of the streamwise intensity as a function of Re_τ up to 10^{10}. These predictions are made at no additional cost using the universal energy density for the inner class of wave parameters and the similarity law for the weight functions. This figure is adapted from figure 8 in Marusic *et al.* (2010*a*) where the DNS and experimental data from channels and boundary layers are summarized (open and filled black symbols). The black filled squares and circles, respectively, show the magnitude of the inner ($y^+ = 15$) and outer ($y^+ = 3.9Re_\tau^{1/2}$) peaks in recent boundary layer experiments (Marusic *et al.* 2010*a*). Using these data, the authors proposed two possibilities for the behavior of the inner peak at high Reynolds numbers. The first possibility is to extrapolate following the trend suggested by the filled black squares (line 1). The second possibility, motivated by the fact that the large scales increase the energy of the small scales, is to extrapolate following line 3 which is parallel to line 2 that captures the variation of the outer peak with Re_τ. Notice that the available data is not sufficient to identify the correct behavior of the inner peak as Re_τ increases. On the other hand, the red circles represent a viable model-based prediction of the inner peak at high Reynolds numbers. These results are obtained for channels and are potentially different than boundary layers. Our ongoing research, to be reported elsewhere, shows that in addition to the inner peak, one can also predict the streamwise intensity in the logarithmic region at arbitrary high Reynolds numbers using the universality of $E_{uu}(y;\kappa_x,\kappa_z,c)$.

5. Concluding remarks

Starting from the NSE, we highlighted the low-rank nature of the resolvent, formulated for individual wall-parallel wavenumbers and frequencies, and illustrated its power by showing that the most energetic motions of real turbulent flows correspond to wavenumbers and frequencies whose resolvent is approximately rank-1 (in the wall-normal direction). Motivated by this observation, we studied the streamwise energy density of the rank-1 model subject to forcings in the wall-parallel directions and time that were broadband and optimized, or "trained", with respect to the available DNS data.

It was shown that the resolvent admits three classes of wavenumbers and wave speeds where the corresponding principal singular values and singular functions exhibit universal behavior with Reynolds number. These classes are directly related to the universal regions of the turbulent mean velocity (which is assumed known *a priori*) and thus are primarily distinguished by the wave speed: (i) a truly inner-scaled class of waves with constant speeds in the inner region of the turbulent mean velocity; (ii) a class of waves with outer-scaled length and constant defect speeds relative to geometric mean of the logarithmic region of the turbulent mean velocity; and (iii) a class of waves with outer-scaled height and width and constant defect speeds relative to the centerline.

The proposed analysis effectively divides the streamwise energy density of the rank-1 model with broadband forcing into three universal regions and enables its scaling to arbitrary large Reynolds numbers. In addition, it was shown that the most energetic wave parameters and the corresponding scales roughly agree with the dominant near-wall motions in real turbulent flows. A weighted energy density was proposed to account for a non-broadband forcing in the wave speed. We illustrated that the weight functions can be optimally shaped such that the weighed energy density of the rank-1 model matches the energy intensity of real turbulent flows at low Reynolds numbers.

As the Reynolds number increases, the optimal weight functions increase for wave speeds in the inner region of the mean velocity. Representation of the optimal weights using similarity laws revealed that the amount of upward shift is linearly correlated with the weight function for wave speeds in the logarithmic region of the mean velocity. In other words, the weight function increases with the energy intensity of the large scales and amplifies the universal inner-scaled energy density of the rank-1 model. Therefore, it implicitly captures the well-known coupling of small scales with the large scales and their subsequent amplification in real turbulent flows. One of the main results of this study is that the rank-1 approximation, together with the optimal weight functions and the (well-known) mean velocity profile, is sufficient for predicting the streamwise energy intensity at high Reynolds numbers.

Our ongoing research, to be reported elsewhere, is focused on the analytical expression of the streamwise energy density for wave speeds in the logarithmic region of the mean velocity and *a priori* derivation of the weight functions. Addressing the limitations and implications of the low-rank model for predicting the wall-normal and spanwise energy spectra as well as the Reynolds stresses is another topic of future research.

Acknowledgments

The support of Air Force Office of Scientific Research under grants FA 9550-09-1-0701 (P.M. John Schmisseur) and FA 9550-12-1-0469 (P.M. Doug Smith) is gratefully acknowledged.

Appendix A. Derivation of the Reynolds number scalings

We derive the classes of wave parameters that induce universal behavior on the low-rank approximation of H.

A.1. *The intrinsic inner class*

Consider the inner coordinate where all spatial coordinates are scaled with the viscous unit ν/u_τ

$$x^+ = Re_\tau x, \quad y^+ = Re_\tau y, \quad z^+ = Re_\tau z.$$

The differential operators in y and the wavenumber symbols in the inner coordinates are

$$\partial/\partial_{y^+} = Re_\tau^{-1}\partial/\partial_y, \quad \kappa_x^+ = Re_\tau^{-1}\kappa_x, \quad \kappa_z^+ = Re_\tau^{-1}\kappa_z, \quad \Delta^+ = Re_\tau^{-2}\Delta.$$

Consequently in the inner coordinates, the operators R_A, C, and $C^\dagger$ in (3.1) scale as

$$\begin{aligned} R_A &= \begin{bmatrix} Re_\tau X_1 & 0 \\ Re_\tau^2 X_3 & Re_\tau X_2 \end{bmatrix}^{-1} = \begin{bmatrix} Re_\tau^{-1} Y_1 & 0 \\ Y_3 & Re_\tau^{-1} Y_2 \end{bmatrix}, \\ C &= \begin{bmatrix} C_1 & Re_\tau^{-1} C_2 \\ C_3 & 0 \\ C_4 & Re_\tau^{-1} C_5 \end{bmatrix}, \quad C^\dagger = \begin{bmatrix} C_1^\dagger & C_3^\dagger & C_4^\dagger \\ Re_\tau C_2^\dagger & 0 & Re_\tau C_5^\dagger \end{bmatrix}. \end{aligned} \tag{A 1}$$

For given κ_x^+ and κ_z^+, the operators C_1 to C_5 and their adjoints are independent of Re_τ. On the other hand, the operators X_1 to X_3 and Y_1 to Y_3 contain spatially-varying coefficients, $U - c$ and its first two derivatives, that depend on Re_τ. As discussed in the beginning of § 3, U scales with y^+ and is independent of Re_τ for $y^+ \lesssim 100$. Therefore, for given κ_x^+, κ_z^+, and $c \lesssim U(y^+ = 100) = 16$, the operators X_1 to X_3 and Y_1 to Y_3 are independent of Re_τ when acting on functions whose supports are inside the interval $0 < y^+ \lesssim 100$. Since the principal singular functions of H are localized around the critical layer (i.e. the wall-normal location where the turbulent mean velocity equals c), the singular functions of H are negligible outside $y^+ \lesssim 100$ for $c \lesssim 16$ and all of the aforementioned operators are effectively independent of Re_τ. It follows from (A 1) that

$$H = CR_AC^\dagger = \begin{bmatrix} Re_\tau^{-1} H_{11} & Re_\tau^{-1} H_{12} & Re_\tau^{-1} H_{13} \\ Re_\tau^{-1} H_{21} & Re_\tau^{-1} H_{22} & Re_\tau^{-1} H_{23} \\ Re_\tau^{-1} H_{31} & Re_\tau^{-1} H_{32} & Re_\tau^{-1} H_{33} \end{bmatrix},$$

where the operators H_{ij} are effectively independent of Re_τ when acting on their principal singular functions. Therefore, the principal singular value of H is proportional to Re_τ^{-1}. In addition, the orthonormality constraints (2.9) on $\hat{\boldsymbol{\psi}}_1$ and $\hat{\boldsymbol{\phi}}_1$ require that these functions scale as $Re_\tau^{1/2}$. This is because the supports of $\hat{\boldsymbol{\psi}}_1$ and $\hat{\boldsymbol{\phi}}_1$ are independent of Re_τ in inner units (hence, proportional to Re_τ^{-1} in outer units). In other words, $\hat{\boldsymbol{\psi}}_1(y)$ and $\hat{\boldsymbol{\phi}}_1(y)$ become thinner and taller as Re_τ increases. Finally, the streamwise energy density $E_{uu} = \kappa_x^2 \kappa_z \sigma_1^2 |u_1|^2$ scales with

$$\left(Re_\tau\right)^2 \left(Re_\tau\right) \left(Re_\tau^{-1}\right)^2 \left(Re_\tau^{1/2}\right)^2 = Re_\tau^2.$$

A.2. *The intrinsic outer-in-x class*

Consider the outer-in-x coordinates where x is scaled with the outer unit h and y and z are scaled with the geometric mean of the inner and outer units. The wall-normal differential operators and the spanwise wavenumber symbol in the outer-in-x coordinates are given by

$$\partial/\partial_{\breve{y}} = Re_\tau^{-1/2}\partial/\partial_y, \quad \breve{\kappa}_z = Re_\tau^{-1/2}\kappa_z.$$

For given κ_x and $\check{\kappa}_z$, the Laplacian

$$\Delta \;=\; Re_\tau \partial_{\check{y}\check{y}} \;-\; \kappa_x^2 \;-\; Re_\tau(\check{\kappa}_z)^2,$$

approximately scales with Re_τ if $Re_\tau(\check{\kappa}_z)^2$ dominates κ_x^2 for all values of Re_τ. It suffices that this condition is satisfied for the smallest Reynolds number $Re_{\tau,\min}$ that is considered. This requires

$$\frac{\lambda_x}{\check{\lambda}_z} \;=\; \frac{\check{\kappa}_z}{\kappa_x} \gtrsim \sqrt{\frac{10}{Re_{\tau,\min}}}. \tag{A 2}$$

In the outer-in-x coordinates, the operators R_A, C, and $C^\dagger$ scale as

$$\begin{aligned} R_A \;&\approx\; \begin{bmatrix} \check{X}_1 & 0 \\ Re_\tau \check{X}_3 & \check{X}_2 \end{bmatrix}^{-1} = \begin{bmatrix} \check{Y}_1 & 0 \\ Re_\tau \check{Y}_3 & \check{Y}_2 \end{bmatrix}, \\ C \;&\approx\; \begin{bmatrix} Re_\tau^{-1/2}\check{C}_1 & Re_\tau^{-1/2}\check{C}_2 \\ \check{C}_3 & 0 \\ \check{C}_4 & Re_\tau^{-1}\check{C}_5 \end{bmatrix}, \quad C^\dagger \;\approx\; \begin{bmatrix} Re_\tau^{-1/2}\check{C}_1^\dagger & \check{C}_3^\dagger & \check{C}_4^\dagger \\ Re_\tau^{1/2}\check{C}_2^\dagger & 0 & \check{C}_5^\dagger \end{bmatrix}. \end{aligned} \tag{A 3}$$

For given κ_x and $\check{\kappa}_z$ that satisfy the constraint (A 2), the operators $\check{C}_1$ to $\check{C}_5$ and their adjoints are approximately independent of Re_τ. We recall from figure 6(c) that $U(\check{y})-U_m$, with U_m denoting the mean velocity at the geometric mean of the logarithmic region, is independent of Re_τ for $50/\sqrt{Re_{\tau,\min}} \lesssim \check{y} \lesssim 0.2\sqrt{Re_{\tau,\min}}$. Therefore, for given κ_x, $\check{\kappa}_z$, and $|U_m - c| \lesssim (1/2\kappa)\log(Re_{\tau,\min}(50/0.2))$, the operators $\check{X}_1$ to $\check{X}_3$ and $\check{Y}_1$ to $\check{Y}_3$ are approximately independent of Re_τ when acting on functions whose supports are inside the interval $50/\sqrt{Re_{\tau,\min}} \lesssim \check{y} \lesssim 0.2\sqrt{Re_{\tau,\min}}$. Following (A 3) and using the locality of the principal singular functions of H around the critical layer, we have

$$H \;=\; CR_AC^\dagger \;\approx\; \begin{bmatrix} \check{H}_{11} & Re_\tau^{1/2}\check{H}_{12} & Re_\tau^{1/2}\check{H}_{13} \\ Re_\tau^{-1/2}\check{H}_{21} & \check{H}_{22} & \check{H}_{23} \\ Re_\tau^{-1/2}\check{H}_{31} & \check{H}_{32} & \check{H}_{33} \end{bmatrix},$$

where the operators $\check{H}_{ij}$ are approximately independent of Re_τ when acting on their principal singular functions. Therefore, the principal singular value of H is proportional to $Re_\tau^{1/2}$. In addition, since $\hat{\boldsymbol{\psi}}_1$ and $\hat{\boldsymbol{\phi}}_1$ scale in $\check{y}$, the orthonormality constraints (2.9) require that these functions be proportional to $Re_\tau^{1/4}$. Then, the streamwise energy density $E_{uu} = \kappa_x^2\kappa_z\sigma_1^2|u_1|^2$ scales with

$$\left(1\right)^2 \left(Re_\tau^{1/2}\right) \left(Re_\tau^{1/2}\right)^2 \left(Re_\tau^{1/4}\right)^2 \;=\; Re_\tau^2.$$

A.3. *The intrinsic outer-in-y class*

Consider the outer-in-y coordinates where y and z are scaled with h and x is scaled hRe_τ. The streamwise wavenumber symbol in the outer-in-y coordinates is given by $\kappa_x^- = Re_\tau\kappa_x$. The Laplacian

$$\Delta \;=\; \partial_{yy} \;-\; Re_\tau^{-2}(\kappa_x^-)^2 \;-\; \kappa_z^2,$$

is independent of Re_τ if κ_z^2 dominates $Re_\tau^{-2}(\kappa_x^-)^2$ for all values of Re_τ. For fixed κ_x^- and κ_z, it suffices that

$$\frac{\lambda_x^-}{\lambda_z} \;=\; \frac{\kappa_z}{\kappa_x^-} \gtrsim \frac{\sqrt{10}}{Re_{\tau,\min}}. \tag{A 4}$$

In the outer-in-y coordinates, the operators R_A, C, and $C^\dagger$ scale as

$$\begin{aligned} R_A &\approx \begin{bmatrix} Re_\tau^{-1}\tilde{X}_1 & 0 \\ \tilde{X}_3 & Re_\tau^{-1}\tilde{X}_2 \end{bmatrix}^{-1} = \begin{bmatrix} Re_\tau\tilde{Y}_1 & 0 \\ Re_\tau^2\tilde{Y}_3 & Re_\tau\tilde{Y}_2 \end{bmatrix}, \\ C &\approx \begin{bmatrix} Re_\tau^{-1}\tilde{C}_1 & \tilde{C}_2 \\ \tilde{C}_3 & 0 \\ \tilde{C}_4 & Re_\tau^{-1}\tilde{C}_5 \end{bmatrix}, \quad C^\dagger \approx \begin{bmatrix} Re_\tau^{-1}\tilde{C}_1^\dagger & \tilde{C}_3^\dagger & \tilde{C}_4^\dagger \\ \tilde{C}_2^\dagger & 0 & Re_\tau^{-1}\tilde{C}_5^\dagger \end{bmatrix}. \end{aligned} \tag{A 5}$$

For given κ_x^- and κ_z that satisfy the constraint (A 4), the operators $\tilde{C}_1$ to $\tilde{C}_5$ and their adjoints are approximately independent of Re_τ. In addition, the defect velocity $U_{cl}-U(y)$ is independent of Re_τ for $y \gtrsim 0.1$. Therefore, for given κ_x^-, κ_z, and $U_{cl}-c \lesssim U_{cl}-U(y=0.1)=6$, the operators $\tilde{X}_1$ to $\tilde{X}_3$ and $\tilde{Y}_1$ to $\tilde{Y}_3$ are approximately independent of Re_τ when acting on functions whose supports are inside the interval $0.1 \lesssim y \lesssim 1$. From (A 5), we have

$$H = CR_AC^\dagger \approx \begin{bmatrix} Re_\tau\tilde{H}_{11} & Re_\tau^2\tilde{H}_{12} & Re_\tau^2\tilde{H}_{13} \\ \tilde{H}_{21} & Re_\tau\tilde{H}_{22} & Re_\tau\tilde{H}_{23} \\ \tilde{H}_{31} & Re_\tau\tilde{H}_{32} & Re_\tau\tilde{H}_{33} \end{bmatrix}. \tag{A 6}$$

Owing to the locality of the principal singular functions around the critical layer, the operators $\tilde{H}_{ij}$ are approximately independent of Re_τ when acting on their principal singular functions. Therefore, the principal singular value of H is proportional to Re_τ^2. Since $\hat{\boldsymbol{\psi}}_1$ and $\hat{\boldsymbol{\phi}}_1$ scale in the outer length scale, the orthonormality constraints (2.9) require that these functions be independent of Re_τ. Finally, the streamwise energy density $E_{uu}=\kappa_x^2\kappa_z\sigma_1^2|u_1|^2$ scales with

$$\left(Re_\tau^{-1}\right)^2\left(1\right)\left(Re_\tau^2\right)^2\left(1\right)^2 = Re_\tau^2.$$

REFERENCES

Adrian, R. J. 2007 Hairpin vortex organization in wall turbulence. *Phys. Fluids* **19**, 041301.

Adrian, R. J., Meinhart, C. D. & Tomkins, C. D. 2000 Vortex organization in the outer region of the turbulent boundary layer. *J. Fluid Mech.* **422**, 1–54.

Afzal, N. 1984 Mesolayer theory for turbulent flows. *AIAA Journal* **22**, 437–439.

Balakumar, B. J. & Adrian, R. J. 2007 Large-and very-large-scale motions in channel and boundary-layer flows. *Phil. Trans. R. Soc. London, Ser. A* **365**, 665–681.

Bamieh, B. & Dahleh, M. 2001 Energy amplification in channel flows with stochastic excitation. *Phys. Fluids* **13** (11), 3258–3269.

Bourguignon, J.-L., Sharma, A. S., Tropp, J. A. & McKeon, B. J. 2013 Compact representation of wall-bounded turbulence using compressive sampling. *(In preparation)* .

Butler, K. M. & Farrell, B. F. 1992 Three-dimensional optimal perturbations in viscous shear flow. *Phys. Fluids A* **4**, 1637.

Butler, K. M. & Farrell, B. F. 1993 Optimal perturbations and streak spacing in wall-bounded turbulent shear flow. *Phys. Fluids A* **5** (3), 774–777.

Cess, R. D. 1958 A survey of the literature on heat transfer in turbulent tube flow. *Westinghouse Research, Rep. 8-0529-R24* .

Chung, D. & McKeon, B. J. 2010 Large-eddy simulation investigation of large-scale structures in a long channel flow. *J. Fluid Mech.* **661**, 341–364.

Coles, D. E. 1956 The law of the wake in the turbulent boundary layer. *J. Fluid Mech.* **1**, 191–226.

CVX Research, Inc. 2012 CVX: Matlab software for disciplined convex programming, version 2.0 beta. `http://cvxr.com/cvx`.

del Álamo, J. C. & Jiménez, J. 2006 Linear energy amplification in turbulent channels. *J. Fluid Mech.* **559**, 205–213.

del Álamo, J. C. & Jiménez, J. 2009 Estimation of turbulent convection velocities and corrections to Taylor's approximation. *J. Fluid Mech.* **640**, 5–26.

del Álamo, J. C., Jiménez, J., Zandonade, P. & Moser, R. D. 2004 Scaling of the energy spectra of turbulent channels. *J. Fluid Mech.* **500**, 135–144.

Farrell, B. F. & Ioannou, P. J. 1993*a* Optimal excitation of three-dimensional perturbations in viscous constant shear flow. *Phys. Fluids A* **5** (6), 1390–1400.

Farrell, B. F. & Ioannou, P. J. 1993*b* Stochastic forcing of the linearized Navier-Stokes equations. *Phys. Fluids A* **5** (11), 2600–2609.

Farrell, B. F. & Ioannou, P. J. 1998 Perturbation structure and spectra in turbulent channel flow. *Theoret. Comput. Fluid Dynamics* **11**, 237–250.

Gad-El-Hak, M. & Bandyopadhyay, P. R. 1994 Reynolds number effects in wall-bounded turbulent flows. *Appl. Mech. Rev.* **47** (8), 307–365.

Grant, M. & Boyd, S. 2008 Graph implementations for nonsmooth convex programs. In *Recent Advances in Learning and Control* (ed. V. Blondel, S. Boyd & H. Kimura), pp. 95–110. Springer-Verlag Limited, `http://stanford.edu/~boyd/graph_dcp.html`.

Guala, M., Hommema, S. E. & Adrian, R. J. 2006 Large-scale and very-large-scale motions in turbulent pipe flow. *J. Fluid Mech.* **554**, 521–542.

Gustavsson, L. H. 1991 Energy growth of three-dimensional disturbances in plane Poiseuille flow. *J. Fluid Mech.* **98**, 149.

Halko, N., Martinsson, P. G. & Tropp, J. A. 2011 Finding structure with randomness: Probabilistic algorithms for constructing approximate matrix decompositions. *SIAM review* **53** (2), 217–288.

Head, M. R. & Bandyopadhyay, P. 1981 New aspects of turbulent boundary-layer structure. *J. Fluid Mech.* **107**, 297–338.

Hoyas, S. & Jiménez, J. 2006 Scaling of the velocity fluctuations in turbulent channels up to $Re_\tau = 2003$. *Phys. Fluids* **18** (1), 011702.

Hultmark, M., Vallikivi, M., Bailey, S. C. C. & Smits, A. J. 2012 Turbulent pipe flow at extreme Reynolds numbers. *Phys. Rev. Lett.* **108** (9), 94501.

Hutchins, N. & Marusic, I. 2007*a* Evidence of very long meandering features in the logarithmic region of turbulent boundary layers. *J. Fluid Mech.* **579**, 1–28.

Hutchins, N. & Marusic, I. 2007*b* Large-scale influences in near-wall turbulence. *Phil. Trans. R. Soc. London, Ser. A* **365**, 647–664.

Hutchins, N., Monty, J. P., Ganapathisubramani, B., Ng, H. C. H. & Marusic, I. 2011 Three-dimensional conditional structure of a high-Reynolds number turbulent boundary layer. *J. Fluid Mech.* **673**, 255–285.

Hutchins, N., Nickels, T. B., Marusic, I. & Chong, M. S. 2009 Hot-wire spatial resolution issues in wall-bounded turbulence. *J. Fluid Mech.* **635**, 103–136.

Hwang, Y. & Cossu, C. 2010 Linear non-normal energy amplification of harmonic and stochastic forcing in the turbulent channel flow. *J. Fluid Mech.* **664**, 51–73.

Jovanović, M. R. & Bamieh, B. 2005 Componentwise energy amplification in channel flows. *J. Fluid Mech.* **534**, 145–183.

Kim, J. & Hussain, F. 1993 Propagation velocity of perturbations in turbulent channel flow. *Phys. Fluids A* **5**, 695–706.

Kim, J. & Lim, J. 2000 A linear process in wall-bounded turbulent shear flows. *Phys. Fluids* **12** (8), 1885–1888.

Kim, K. C. & Adrian, R. J. 1999 Very large-scale motion in the outer layer. *Phys. Fluids* **11**, 417–422.

Klewicki, J. C. 2010 Reynolds number dependence, scaling, and dynamics of turbulent boundary layers. *J. Fluid Eng.* **132** (9), 094001.

Kline, S. J., Reynolds, W. C., Schraub, F. A. & Runstadler, P. W. 1967 The structure of turbulent boundary layers. *J. Fluid Mech.* **30**, 741–773.

Klingmann, B. G. B. 1992 On transition due to three-dimensional disturbances in plane Poiseuille flow. *J. Fluid Mech.* **240**, 167–195.

Kunkel, G. J. & Marusic, I. 2006 Study of the near-wall-turbulent region of the high-Reynolds-number boundary layer using an atmospheric flow. *J. Fluid Mech.* **548**, 375–402.

Landahl, M. T. 1975 Wave breakdown and turbulence. *SIAM J. Appl. Math.* **28**, 735–756.

LeHew, J., Guala, M. & McKeon, B. J. 2011 A study of the three-dimensional spectral energy distribution in a zero pressure gradient turbulent boundary layer. *Exp. Fluids* **51**, 997–1012.

Long, R. R. & Chen, T. C. 1981 Experimental evidence for the existence of the mesolayer in turbulent systems. *J. Fluid Mech.* **105**, 19–59.

Malkus, W. V. R. 1956 Outline of a theory of turbulent shear flow. *J. Fluid Mech.* **1** (5), 521–539.

Marusic, I. & Kunkel, G. J. 2003 Streamwise turbulence intensity formulation for flat-plate boundary layers. *Phys. Fluids* **15** (8), 2461–2464.

Marusic, I., Mathis, R. & Hutchins, N. 2010*a* High Reynolds number effects in wall turbulence. *Int. J. Heat Fluid Flow* **31**, 418–428.

Marusic, I., Mathis, R. & Hutchins, N. 2010*b* Predictive model for wall-bounded turbulent flow. *Science* **329** (5988), 193–196.

Marusic, I., McKeon, B. J., Monkewitz, P. A., Nagib, H. M., Smits, A. J. & Sreenivasan, K. R. 2010*c* Wall-bounded turbulent flows at high Reynolds numbers: Recent advances and key issues. *Phys. Fluids* **22**, 065103.

Marusic, I., Monty, J. P., Hultmark, M. & Smits, A. J. 2013 On the logarithmic region in wall turbulence. *J. Fluid Mech.* **716**, R3–1 – 716 R3–11.

Mathis, R., Hutchins, N. & Marusic, I. 2009*a* Large-scale amplitude modulation of the small-scale structures in turbulent boundary layers. *J. Fluid Mech.* **628**, 311–337.

Mathis, R., Monty, J. P., Hutchins, N. & Marusic, I. 2009*b* Comparison of large-scale amplitude modulation in turbulent boundary layers, pipes, and channel flows. *Phys. Fluids* **21**, 111703.

Matsubara, M. & Alfredsson, P. H. 2001 Disturbance growth in boundary layers subjected to free-stream turbulence. *J. Fluid Mech.* **430**, 149–168.

McKeon, B. J. & Sharma, A. S. 2010 A critical-layer framework for turbulent pipe flow. *J. Fluid Mech.* **658**, 336–382.

McKeon, B. J., Sharma, A. S. & Jacobi, I. 2013 Experimental manipulation of wall turbulence - a systems approach. *Phys. Fluids* (to appear).

Meseguer, A. & Trefethen, L. N. 2003 Linearized pipe flow to Reynolds number 10^7. *J. Comput. Phys.* **186**, 178–197.

Metzger, M. M. & Klewicki, J. C. 2001 A comparative study of near-wall turbulence in high and low Reynolds number boundary layers. *Phys. Fluids* **13**, 692.

Moarref, R. & Jovanović, M. R. 2012 Model-based design of transverse wall oscillations for turbulent drag reduction. *J. Fluid Mech.* **707**, 205–240.

Monty, J. P. 2005 Developments in smooth wall turbulent duct flows. PhD thesis, University of Melbourne.

Monty, J. P. & Chong, M. S. 2009 Turbulent channel flow: comparison of streamwise velocity data from experiments and direct numerical simulation. *J. Fluid Mech.* **633**, 461–474.

Monty, J. P., Hutchins, N., Ng, H. C. H., Marusic, I. & Chong, M. S. 2009 A comparison of turbulent pipe, channel and boundary layer flows. *J. Fluid Mech.* **632**, 431–442.

Monty, J. P., Stewart, J. A., Williams, R. C. & Chong, M. S. 2007 Large-scale features in turbulent pipe and channel flows. *J. Fluid Mech.* **589**, 147–156.

Morrison, J. F., McKeon, B. J., Jiang, W. & Smits, A. J. 2004 Scaling of the streamwise velocity component in turbulent pipe flow. *J. Fluid Mech.* **508**, 99–131.

Panton, R. L. 2001 Overview of the self-sustaining mechanisms of wall turbulence. *Prog. Aerosp. Sci.* **37** (4), 341–383.

Perry, A. E. & Chong, M. S. 1982 On the mechanism of wall turbulence. *J. Fluid Mech.* **119** (173), 106–121.

Pujals, G., García-Villalba, M., Cossu, C. & Depardon, S. 2009 A note on optimal transient growth in turbulent channel flows. *Phys. Fluids* **21** (1), 015109.

Reddy, S. C. & Henningson, D. S. 1993 Energy growth in viscous channel flows. *J. Fluid Mech.* **252**, 209–238.

Reynolds, W. C. & Hussain, A. K. M. F. 1972 The mechanics of an organized wave in turbulent shear flow. Part 3. Theoretical models and comparisons with experiments. *J. Fluid Mech.* **54** (2), 263–288.

Reynolds, W. C. & Tiederman, W. G. 1967 Stability of turbulent channel flow with application to Malkus's theory. *J. Fluid Mech.* **27** (2), 253–272.

Robinson, S. K. 1991 Coherent motions in the turbulent boundary layer. *Annu. Rev. Fluid Mech.* **23**, 601–639.

Schmid, P. J. 2007 Nonmodal stability theory. *Annu. Rev. Fluid Mech.* **39**, 129–162.

Schmid, P. J. & Henningson, D. S. 1992 A new mechanism for rapid transition involving a pair of oblique waves. *Phys. Fluids A* **4** (9), 1986–1989.

Schmid, P. J. & Henningson, D. S. 2001 *Stability and Transition in Shear Flows*. Springer-Verlag.

Sharma, A. S. & McKeon, B. J. 2012 On coherent structure in wall turbulence. *J. Fluid Mech.* Submitted, also http://arxiv.org/abs/1301.7580.

Smith, C. R. & Metzler, S. P. 1983 The characteristics of low-speed streaks in the near-wall region of a turbulent boundary layer. *J. Fluid Mech.* **129**, 27–54.

Smits, A. J., McKeon, B. J. & Marusic, I. 2011 High-Reynolds number wall turbulence. *Annu. Rev. Fluid Mech.* **43**, 353–375.

Sreenivasan, K. R. & Sahay, A. 1997 The persistence of viscous effects in the overlap region, and the mean velocity in turbulent pipe and channel flows. pp. 253–272.

Taylor, G. 1938 The spectrum of turbulence. *Proc. R. Soc. Lond. A* **164** (919), 476–490.

Townsend, A. 1976 *The structure of turbulent shear flow*. Cambridge University Press.

Trefethen, L. N., Trefethen, A. E., Reddy, S. C. & Driscoll, T. A. 1993 Hydrodynamic stability without eigenvalues. *Science* **261**, 578–584.

Wei, T., Fife, P., Klewicki, J. & McMurtry, P. 2005 Properties of the mean momentum balance in turbulent boundary layer, pipe and channel flows. *J. Fluid Mech.* **522**, 303–327.

Weideman, J. A. C. & Reddy, S. C. 2000 A MATLAB differentiation matrix suite. *ACM Transactions on Mathematical Software* **26** (4), 465–519.